mathematics

MDPI

Article

Optimal Control of a Small Flexible Aircraft Using an Active Gust Alleviation Device

Yanxuan Wu *, Yifan Fu, Hao Li, Xudong Luo and Haonan Sun

School of Mechatronics Engineering, Beijing Institute of Technology, Beijing 100081, China; 3120240168@bit.edu.cn (Y.F.); 3120230168@bit.edu.cn (H.L.); 3120250242@bit.edu.cn (X.L.); 3220250212@bit.edu.cn (H.S.)

* Correspondence: alexwyx@bit.edu.cn

Abstract

Small flexible-wing aircraft are vulnerable to gusts due to their low inertia and operating regime at low-Reynolds-number regimes, compromising flight stability and mission reliability. This paper introduces a novel active gust alleviation device (AGAD) installed at the wingtip, which works in concert with the conventional tail-plane to form a multi-surface control system. To coordinate these surfaces optimally, a quasi-static aeroelastic aircraft model is established, and a linear–quadratic regulator (LQR) controller is designed. A key innovation is the integration of an extended state observer (ESO) to estimate the unmeasurable, gust-induced angle of attack in real time, allowing the LQR to effectively counteract unsteady disturbances. Comparative simulations against a baseline (tail-plane-only control) demonstrate the superiority of the combined AGAD-tail strategy: the peak gust responses in pitch angle and normal acceleration are reduced by over 57% and 20%, respectively, while structural loads at the wing root are also significantly attenuated. Furthermore, the AGAD enhances maneuverability, reducing climb time by 20% during a specified maneuver. This study confirms that the integrated AGAD and LQR-ESO framework provides a practical and effective solution for enhancing both the stability and agility of small flexible aircraft in gusty environments, with direct benefits for applications like precision inspection and monitoring.

Keywords: flight dynamics; aeroelasticity; gust alleviation; active gust alleviation device; optimal control

MSC: 49N10; 93B53

check for updates

Academic Editor: Aydin Azizi

Received: 21 November 2025
Revised: 10 December 2025
Accepted: 12 December 2025
Published: 14 December 2025

Citation: Wu, Y.; Fu, Y.; Li, H.; Luo, X.; Sun, H. Optimal Control of a Small Flexible Aircraft Using an Active Gust Alleviation Device. *Mathematics* **2025**, *13*, 3986. https://doi.org/10.3390/math13243986

Copyright: © 2025 by the authors. Licensee MDPI, Basel, Switzerland. This article is an open access article distributed under the terms and conditions of the Creative Commons Attribution (CC BY) license (https://creativecommons.org/licenses/by/4.0/).

1. Introduction

In recent years, small flexible-wing aircraft have demonstrated significant potential for low-altitude urban missions due to their superior maneuverability and adaptability [1]. However, their operation at low Reynolds numbers (typically on the order of 10^4 to 10^5) involves complex aerodynamic phenomena, and their lightweight, low-inertia nature makes them highly susceptible to atmospheric disturbances, particularly wind gusts, which critically compromise flight stability and structural integrity [2–7]. Consequently, developing effective gust alleviation techniques is paramount for the reliable deployment of this class of vehicles [8–15].

Gust alleviation strategies are broadly categorized as passive or active [16]. Passive methods, such as exploiting composite anisotropy or structural tailoring, inherently improve aeroelastic response but lack adaptability to varying flight conditions [17–19]. Active

methods, in contrast, modify aerodynamic load distribution in real-time by actuating control surfaces, offering greater environmental adaptability and performance potential [20]. Current research frontiers converge on two interrelated directions: innovations in aerodynamic configuration and evolution in control strategy.

Regarding aerodynamic configuration, actively controlled wingtip devices have become a focal point due to their ability to dramatically alter wing load distribution. Early investigations explored the potential of multi-flap systems like the Variable Camber Continuous Trailing Edge (VCCTE) [21–25]. Similarly, the University of Washington designed the large flexible wing (LFW) wind-tunnel model with active trailing-edge flaps [26,27]. Recently, the focus has shifted toward more integrated and dynamically responsive wingtip designs. For instance, Healy et al. conducted an in-depth experimental and numerical study on the nonlinear dynamics of a flared folding wingtip (FFWT), revealing complex behaviors like limit cycle oscillations beyond the flutter boundary, and introduced active control via a wingtip trim tab [28]. Ahmadi-Tehrani et al. directly addressed gust load alleviation through wind-tunnel tests of an active controlled folding wingtip (ACFWT), demonstrating its effectiveness using classical PD and PID control strategies [29]. In parallel, other research has advanced the fundamental modeling of such devices. Recent work has developed a nonlinear aeroelastic framework coupling multibody dynamics with an Unsteady Vortex Lattice Method (UVLM) specifically for FFWTs, explicitly accounting for the geometric nonlinearities of large folding angles often neglected in linear analyses. This approach has been validated against wind-tunnel gust response tests, highlighting the significant influence of nonlinearities on the wingtip's dynamic response, especially under low-frequency excitation [30].

Concerning control strategies, research has evolved from classical to modern optimal and robust control. For novel configurations, Balatti et al. implemented a PD controller on a hinged wingtip in simulation [31]. However, for a multivariable, strongly coupled flexible aircraft system, advanced strategies like model predictive control (MPC) have garnered significant attention due to their ability to explicitly handle constraints and perform multi-objective optimization. Narimani et al. applied MPC to an FFWT, optimizing the wing root bending moment over a prediction horizon and achieving superior gust load reduction compared to PID [32]. Extending MPC to more complex, flexible airframes, recent work has demonstrated a practical framework for gust load alleviation on flexible flying wings. By employing a reduced-order linear parameter-varying (LPV) model and efficient optimization, it balances performance with computational tractability, showcasing the real-time potential of advanced control for complex aeroelastic systems [33]. Nevertheless, algorithms like MPC demand considerable computational resources and accurate models, posing challenges for implementation on resource-constrained small platforms [34–36].

In summary, while significant progress has been made in both aerodynamic configurations and control algorithms, a discernible gap remains: the lack of an integrated solution specifically designed for small, low-cost, resource-constrained flexible aircraft platforms that balances high performance with low computational complexity. Most advanced control studies target larger platforms or assume substantial computational capability, often overlooking the practical constraints of small aircraft.

To bridge this gap, the core contribution of this work lies in the novel integration of an AGAD at the wingtip with conventional tail-plane control within an LQR-ESO framework, tailored specifically for small flexible aircraft operating in gust-prone environments. This research employs an ESO to estimate the unmeasurable gust-induced angle of attack, enabling effective compensation for external aerodynamic disturbances. Furthermore, a two-layer control architecture is introduced, comprising an upper command generator that translates flight tasks into optimal tracking signals and a lower LQR controller that

coordinates the AGAD and tail-plane for simultaneous gust alleviation and maneuver tracking. This integrated approach demonstrates significant improvements in flight stability, structural load reduction, and maneuverability, offering a practical and robust solution for resource-constrained micro-aerial vehicles.

To clearly demonstrate the effectiveness of the proposed AGAD control strategy, a comparative study is set up between two configurations: baseline and AGAD configuration. The former represents the conventional control approach where gust alleviation and flight control are managed exclusively by the all-movable tail-plane. The AGAD is locked and does not function as a control surface. The latter embodies the novel approach introduced in this paper, where the AGAD is actively controlled in coordination with the tail-plane under the optimal LQR framework. This direct comparison is designed to isolate and quantify the performance benefits attributable solely to the introduction of the AGAD and its integrated control logic.

The remainder of this paper is organized as follows: Section 2 presents the integrated dynamic model of the flexible-wing aircraft equipped with the AGAD and outlines the LQR control design. Section 3 provides simulations and analysis of gust response and flight performance to validate the proposed approach. Finally, concluding remarks and future works are given in Sections 4 and 5.

2. The Control Method for the Aircraft with AGAD

The AGAD, in the form of a rigid control panel, is part of the wing and an alternative control surface, as shown in Figure 1. The AGAD is mounted at the wingtip through a shaft driven by an actuator to control the rotation angle. By setting the shaft axis in a proper chord-wise location on the AGAD and the tip of the inner wing, the AGAD will be able to alter the wing aerodynamic force and pitching moment to actively control the aircraft's performance. Figure 1 shows the finite element model of a flexible wing structure, which is a beam model arranged along the elastic axis of the wing. There is a structural node possessing three degrees of freedom on each section: vertical displacement, bending angle, and twist angle. Through this model, we can calculate the mass matrix and stiffness matrix of the wing, as detailed in [37].

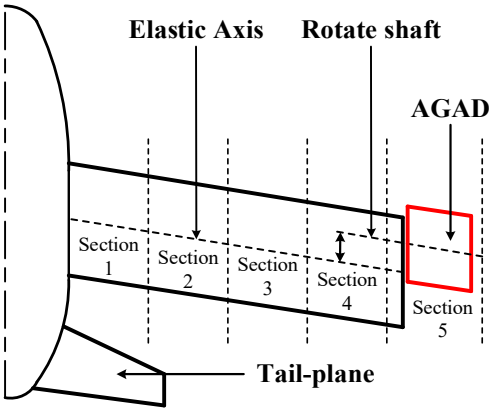


Figure 1. Schematic diagram of the AGAD.

The aircraft flight attitude is mainly controlled by the tail-plane, which also influences normal acceleration. The control of the AGAD is thus coordinated with the wing deformation and tail-plane control simultaneously, as illustrated in Figure 2.

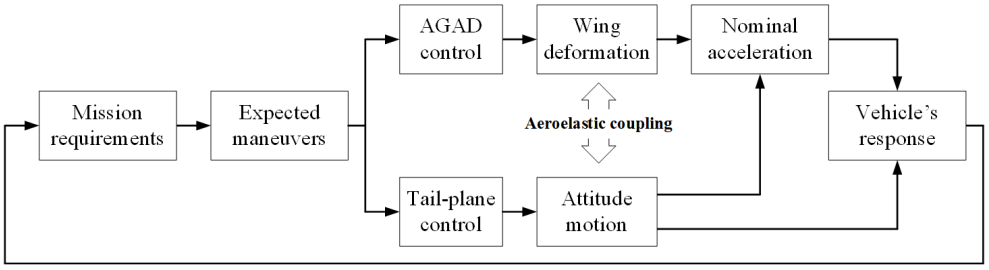


Figure 2. Control logic diagram of flexible-wing aircraft with AGAD tail-plane.

Specifically, the control system for small flexible aircraft equipped with AGAD consists of two main components, as illustrated in Figure 3. The first part is an LQR controller, which tracks the expected system response using the AGAD and the tail-plane. The flexible wing dynamic response and the measured rigid-body response are combined to form the overall system response. The second part is an ESO, designed to estimate the angle of attack (AoA). Its inputs include the system response and the control inputs from both the AGAD and tail-plane. In this paper, the AoA is defined relative to the CG of the aircraft.

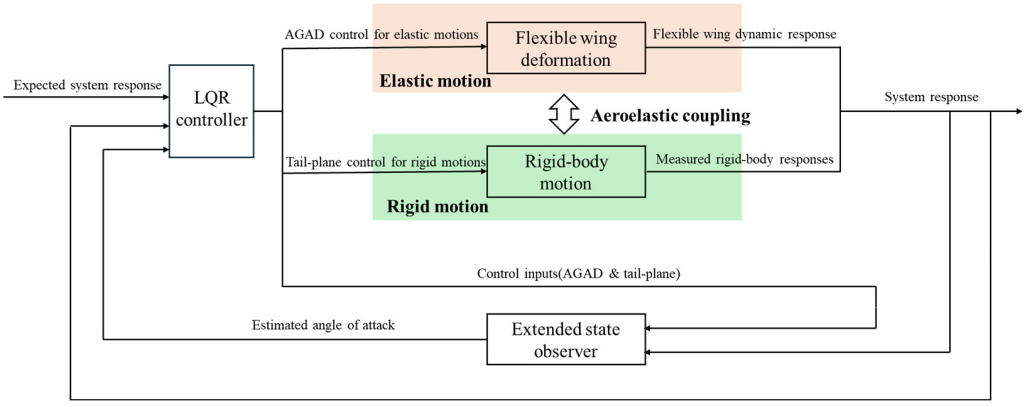


Figure 3. The control system of the flexible-wing aircraft with AGAD.

There are three main objectives to achieve in the design of this control system. Firstly, a simplified low-order control model is created that takes the quasi-static aeroelastic effect of the flexible wing into account. Secondly, the LQR controller is designed to alleviate the gust load and meet the maneuver requirement by using the AGAD and tail-plane in an optimal combination. Finally, a method based on ESO is developed to estimate the equivalent AoA caused by gust load.

2.1. Integrated Aircraft Dynamic Model

By adopting the residualized model method [38–41], the flexible-wing aircraft state-space model of longitudinal dynamic motion, including the wing aeroelastic effect, can be given by

$$\begin{bmatrix} \dot{\boldsymbol{x}}_R \\ \dot{\boldsymbol{x}}_U \end{bmatrix} = \begin{bmatrix} A_{RR} & A_{RE} \\ A_{ER} & A_{EE} \end{bmatrix} \begin{bmatrix} \boldsymbol{x}_R \\ \boldsymbol{x}_U \end{bmatrix} + \begin{bmatrix} B_{RR} & B_{RE} \\ B_{ER} & B_{EE} \end{bmatrix} \boldsymbol{u}(t) \tag{1}$$

where $\boldsymbol{x}_R(t) = [\alpha(t), q(t), \theta(t)]^T$ is the state vector of aircraft rigid-body motion; $\alpha(t)$ represents AoA; and $q(t)$ and $\theta(t)$ represent the angular speed and angle in pitch motion, respectively. $\boldsymbol{x}_U(t) = [x_E, \dot{x}_E]$ is the state vector of the structural elastic deflection of the wing, which contains structural deformation displacement and structural deformation velocity. x_E and $\dot{x}_E$ only contain three mode shapes since the contribution of higher-order modes to elastic deformation is negligible due to their high frequencies (Appendix A.1/Table A1). $\boldsymbol{u}(t) = [\delta e(t), \delta a(t)]^T$ is the control input vector, in which $\delta e(t)$ and $\delta a(t)$ are the input rotation

angles for the tail-plane and the AGAD, respectively. A_{RR} and A_{EE} represent the state matrices for the aircraft rigid-body motion and structural elastic deflection, respectively. A_{RE} and A_{ER} are the state matrices of coupling between the rigid-body motion and elastic deflection. B_{RR}, B_{RE}, B_{ER}, and B_{EE} are the input matrices for the aircraft motion control, including both rigid-body and structural elastic deflection effects.

If we expand the x_U term in Equation (1), then it can be rephrased as follows:

$$\begin{pmatrix} \dot{x}_R \\ \dot{x}_E \\ \ddot{x}_E \end{pmatrix} = \begin{pmatrix} A_{RR} & A_{RE-1} & 0 \\ 0 & 0 & I \\ A_{ER-2} & A_{EE-21} & A_{EE-22} \end{pmatrix} \begin{pmatrix} x_R \\ x_E \\ \dot{x}_E \end{pmatrix} + \begin{pmatrix} B_{RR} & B_{RE} \\ \mathbf{0} & \mathbf{0} \\ B_{ER} & B_{EE} \end{pmatrix} \boldsymbol{u}(t) \tag{2}$$

where $[A_{RE-1}\ 0] = [A_{RE-1}\ A_{RE-2}] = A_{RE}$, $[0\ A_{ER-2}] = A_{ER}$. Due to the lower flight speed and smaller deformation amplitude of the flexible wing structure, quasi-steady aerodynamic forces dominate. The vortex lattice method is used to calculate quasi-steady aerodynamic forces [42]. When only considering quasi-steady aerodynamic forces, the submatrix, A_{RE-2}, related to structural deformation velocity, $\dot{x}_E$, is 0.

Deformation of the membrane wing structure (x_E) can be divided into two parts: instantaneous equilibrium deformation of the membrane wing structure (x_{EB}) and residual deformation of the membrane wing structure ($\widetilde{x}_E$). The modal frequencies of flexible wings are significantly higher than the short-period motion frequency of the aircraft, and our calculation results have once again verified this point; the specific calculation results are included in Appendix A.1/Table A1. Therefore, the fast time-varying state variable, $\widetilde{x}_E$, can be ignored. Thus, we obtain a reduced-order model for controller design, which serves as the core model for dynamic analysis and control design in this paper:

$$\dot{\boldsymbol{x}}_R(t) = A\boldsymbol{x}_R(t) + B\boldsymbol{u}(t) \tag{3}$$

where the system matrix, A, and the input matrix, B, are given by the following equation, and the specific derivation process has been added to Appendix A.2 to avoid affecting the main logic of this paper:

$$\begin{cases} A = A_{RR} - A_{RE-1}A_{EE-21}^{-1}A_{ER-2} \\ B = [B_{RR}\ B_{RE}] - A_{RE-1}A_{EE-21}^{-1}[B_{ER}\ B_{EE}] \end{cases} \tag{4}$$

Matrices A and B incorporate aeroelastic coupling through the residualization process, ensuring that the rigid–flexible interactions are adequately represented for control design purposes. The specific expression of terms in A and B is provided in Appendix A.3.

2.2. LQR Controller Design

For the gust alleviation and maneuver control of a flexible-wing aircraft with multiple control surfaces, the LQR is selected as the core control algorithm. Compared to classical PID control, which is inadequate for systematically coordinating multiple actuators and balancing competing objectives, the LQR provides an optimal framework for multi-input coordination based on the established linearized model. It naturally balances these goals through a quadratic cost function. In contrast to sliding mode control, whose potential chattering might excite the flexible structure, the LQR delivers smoother control actions. Furthermore, compared to MPC, which demands high computational resources for online optimization and robust control methods, which are often complex and conservative, an LQR achieves satisfactory performance with a significantly lower computational burden and greater ease of engineering implementation. This makes it particularly suitable for resource-constrained small aircraft platforms.

The LQR controller is chosen for its optimality in minimizing a quadratic cost function for linear systems with multiple control inputs and states. Given that the reduced-order model in Equation (3) is linear and captures the coupled rigid-body and aeroelastic dynamics, LQR provides an effective framework for coordinating the tail-plane and AGAD controls by minimizing a quadratic cost function:

$$J_{controller} = \frac{1}{2}\int_{t_0}^{\infty} \left[\boldsymbol{e}^T(t)Q_1\boldsymbol{e}(t) + \boldsymbol{u}^T(t)Q_2\boldsymbol{u}(t)\right]dt \tag{5}$$

where Q_1 is a design variable that can take any symmetric semipositive definite matrix value, and Q_2 is a design variable that can take any symmetric positive definite matrix value.

The tracking error $\boldsymbol{e}(t)$ is defined as

$$\begin{cases} \boldsymbol{e}(t) = \boldsymbol{z}(t) - \boldsymbol{x}_R(t) \\ \boldsymbol{z}(t) = \begin{bmatrix} \alpha^*(t) & q^*(t) & \theta^*(t) \end{bmatrix}^T \\ \boldsymbol{x}_R(t) = \begin{bmatrix} \alpha(t) & q(t) & \theta(t) \end{bmatrix}^T \end{cases} \tag{6}$$

where $\boldsymbol{z}(t)$ is the tracking signal, and $\boldsymbol{x}_R(t)$ is the system response.

The optimal control input $\boldsymbol{u}^*$ is given by

$$\boldsymbol{u}^*(t) = -Q_2^{-1}B^TP\boldsymbol{x}_R(t) + Q_2^{-1}B^T\boldsymbol{g}(t) \tag{7}$$

in which P can be obtained by solving the Riccati equation, and $\boldsymbol{g}(t)$ can be calculated from the differential equation:

$$PA + A^TP - PBQ_2^{-1}B^TP + Q_1 = 0 \tag{8}$$

$$\dot{\boldsymbol{g}}(t) = -\left[A - BQ_2^{-1}B^TP\right]^T\boldsymbol{g}(t) - Q_1\boldsymbol{z}(t) \tag{9}$$

The tracking signal, $\boldsymbol{z}(t)$, provides the specified target maneuver of the aircraft for the LQR controller based on the current flight condition and performance. The target maneuver is that the aircraft needs to achieve the specified flight performance, such as a specified climb at a certain altitude.

For heave motion, the target maneuver, such as a specified climb rate, can be determined by

$$V_h(t) = V_x sin\theta(t) - V_z(t)cos\theta(t) \approx V_x\theta(t) - V_z(t) \tag{10}$$

where V_h is the vertical velocity of the aircraft defined in a ground global coordinate system with a positive axis in an upward direction; V_x and $-V_z$ are the velocity components measured in the local coordinate system with the x-axis pointing toward the nose direction, the y-axis pointing toward the right-wing direction, and the z-axis pointing below the aircraft; θ is the pitch angle, defined as nose-up positive. Figure 4 clarifies the relationship between these variables.

Assuming V_x is maintained as stable by an independent feedback control loop, the climb acceleration is given below:

$$a_h(t) = V_xq(t) - \dot{V}_z(t) = V_xq(t) + \overline{q}Sm^{-1}C_\alpha\alpha(t) \tag{11}$$

where $\overline{q}$ is the dynamic pressure ($\overline{q}$ = 0.5 ρV^2), S is the wing area, m is the total mass of the aircraft, C_α is the aircraft lift curve slope, and $\alpha(t)$ is the equivalent AoA excluding the geometric AoA set in trimmed flight.

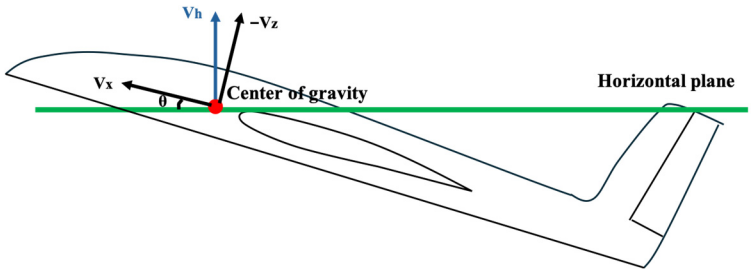


Figure 4. Schematic diagram for heave motion. (Red dot represents center of gravity and green line represents horizontal plane).

For a specified climb acceleration, $a_h(t)$, the relation between the tracking signal of AoA (α^*) and the tracking signal of pitch angular speed (q^*) is given by

$$\alpha^*(t) = [a_h(t) - V_x q^*(t)]\left(\bar{q}Sm^{-1}C_\alpha\right)^{-1} \tag{12}$$

In addition, the tracking signal of pitch angle (θ^*) is defined as

$$\theta^*(t) = \theta(t) + \mu q^*(t)\Delta T \tag{13}$$

where $\theta(t)$ is the aircraft pitch angle at time t, ΔT is a differential amount of time, and μ is an amplification factor. $\theta^*(t)$ provides an approximate prediction of the pitch angle at time step $\mu\Delta T$ ahead, beyond the moment at time t, to enable the LQR controller to suppress potentially excessive pitch angles in advance when tracking commands, thereby improving the dynamic response quality of the aircraft and preventing excessive control. It depends upon the tracking signal of pitch angular speed, $q^*(t)$. A cost function can be created as follows, and the optimal combination of tracking signals is determined by minimizing the cost function:

$$J_{tracking} = \begin{bmatrix} \alpha^*(t) \\ q^*(t) \\ \theta^*(t) \end{bmatrix}^T \begin{bmatrix} W_\alpha & & \\ & W_q & \\ & & W_\theta \end{bmatrix} \begin{bmatrix} \alpha^*(t) \\ q^*(t) \\ \theta^*(t) \end{bmatrix} \tag{14}$$

where W_α, W_q, and W_θ are the weighting factors. Based on the optimal tracking signals, it is possible for the LQR control system to prevent an excessively large pitch angle by restricting the tracking signal of pitch angular speed, $q^*(t)$.

In summary, the proposed control architecture consists of two functionally distinct layers. The upper command generator layer, governed by Equations (12)–(14), translates flight tasks and operational constraints into a set of time-varying optimal tracking signals $\boldsymbol{z}(t)$. The lower LQR controller layer utilizes the cost function in Equation (5) to drive the aircraft state to optimally track the command from the upper layer.

Figure 5 depicts the whole process of obtaining the tracking signal, $\boldsymbol{z}(t)$.

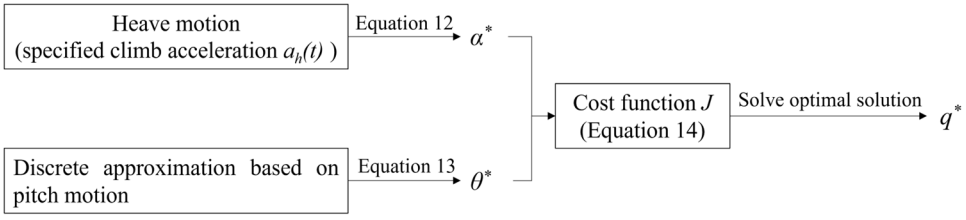


Figure 5. Process of obtaining the tracking signal, $\boldsymbol{z}(t)$.

Combined with Equations (12) and (13), the optimal tracking signals for the LQR controller are given by

$$\begin{gathered} z(t) = \begin{bmatrix} \alpha^*(t) & q^*(t) & \theta^*(t) \end{bmatrix}^T \\ \alpha^*(t) = \left[a_h(t) - V_x q^*(t) \right] \left(\bar{q} S m^{-1} C_\alpha \right)^{-1} \\ q^*(t) = 0.5 K_2 K_1^{-1} \\ \theta^*(t) = \theta(t) + \mu q^*(t) \Delta T \end{gathered} \tag{15}$$

where K_1 and K_2 can be expressed as follows:

$$\begin{gathered} K_1 = W_\alpha V_x^2 \left(\bar{q} S m^{-1} C_\alpha \right)^{-2} + W_q + W_\theta (\mu \Delta T)^2 \\ K_2 = 2 W_\alpha a_h(t) V_x \left(\bar{q} S m^{-1} C_\alpha \right)^{-2} - 2 W_\theta \theta(t) \mu \Delta T \end{gathered} \tag{16}$$

It should be noted that K_2 is an intermediate time-dependent parameter depending upon the aircraft flight speed, attitude, and specified climb acceleration and does not appear in the LQR controller.

According to Equation (16), for a specific climb acceleration, $a_h(t) > 0$, and a predicted excessively large pitch angle, $\theta(t)$, for example, the K_2 would be negative, and $K_1 > 0$. In this case, though the specified maneuver is to climb, there would be a negative tracking signal for the pitch angular speed to be $q^*(t) < 0$. As a result, the LQR controller will command the tail-plane to reduce the likely excessive pitch angle by setting $q(t) < 0$ and actuate the AGAD to achieve the required climb acceleration, $a_h(t) > 0$.

2.3. Evaluation of Equivalent AoA Due to Gust by ESO

AoA is defined as the angle between the air speed vector and the x-axis of the aircraft coordinate system. Our miniaturized low-cost aircraft installs an inertial measurement unit (IMU), which can measure the pitch angle of the aircraft (θ), and a GPS-assisted navigation system, which can measure the flight path angle (γ). The vector difference between θ and γ can characterize the angle between the flight speed vector and the x-axis of the aircraft coordinate system, and we define this angle as the rigid-body motion angle of attack (RAoA, α_r). Flight speed vector is consistent with air speed vector under the still-air assumption, and AoA can be characterized by α_r. However, the vector sum of the air speed vector and vertical gusts is the direction of the aircraft flight speed vector under vertical gusts. That is to say, there is an additional angle induced by gusts between the air speed vector and the aircraft flight speed vector, and we define it as gust-induced angle of attack (GAoA, α_g). Since this angle cannot be measured by onboard equipment, we have designed an ESO to observe it. Consequently, AoA under gusts should be expressed as $\alpha = \alpha_r + \alpha_g$. The relationship between these angles are depicted in Figure 6.

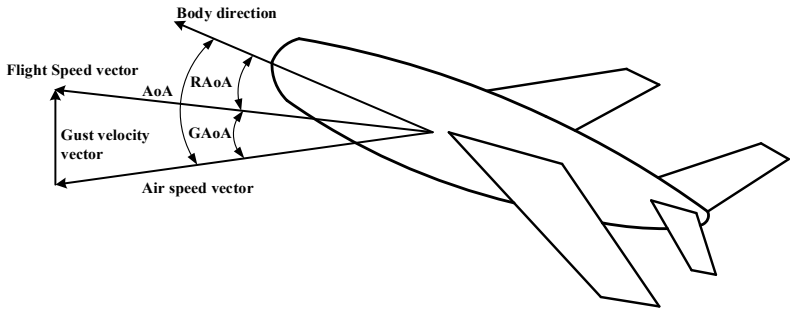


Figure 6. Definition of AoA under gust disturbances.

In order to provide a clear physical derivation basis, we need to specifically expand the state variables and control variables in Equation (3). The more detailed expression of short-period longitudinal motion is given below:

$$\begin{bmatrix} \dot{\alpha}_r \\ \dot{q} \\ \dot{\theta} \end{bmatrix} = \begin{bmatrix} A_{11} & A_{12} & 0 \\ A_{21} & A_{22} & 0 \\ 0 & 1 & 0 \end{bmatrix} \begin{bmatrix} \alpha_r \\ q \\ \theta \end{bmatrix} + \begin{bmatrix} 0 & B_{12} \\ B_{21} & B_{22} \\ 0 & 0 \end{bmatrix} \begin{bmatrix} \delta e \\ \delta a \end{bmatrix} + \begin{bmatrix} A_{11} & -1 \\ A_{21} & 0 \\ 0 & 0 \end{bmatrix} \begin{bmatrix} \alpha_g \\ \dot{\alpha}_g \end{bmatrix} \tag{17}$$

where A_{ii} is the non-zero term of the system matrix, B_{ii} is the non-zero term of the input matrix, and the details of these terms refer to [43]. Therefore, Equation (17) is essentially an equivalent expansion of Equation (3), which explicitly incorporates the GAoA (α_g) and its rate, $\dot{\alpha}_g$, as disturbance inputs, directly affecting the RAoA rate ($\dot{\alpha}_r$) and the pitch acceleration ($\dot{q}$). Physically, $\dot{\alpha}_g$ represents the time-varying component of the vertical gusts, and its inclusion ensures that the model captures not only the instantaneous gust impact but also its dynamic evolution.

For an undisturbed angular movement, according to Equation (17), the angular acceleration is dependent upon flight conditions and control input:

$$\dot{q} = A_{21}\alpha_r + A_{21}\alpha_g + A_{22}q + B_{21}\delta e + B_{22}\delta a \tag{18}$$

When the aircraft encounters gusts, only α_r can be measured by the flight controller through the integrated sensing and navigation system. Although α_g could not be measured, it can be indicated by the aircraft's angular acceleration observed by

$$A_{21}\alpha_g = \dot{q} - (A_{21}\alpha_r + A_{22}q + B_{21}\delta e + B_{22}\delta a) \tag{19}$$

Accurately estimating α_g is critical for effective gust alleviation, yet this state is not directly measurable. Among various estimation algorithms, the ESO is employed for its superior robustness and adaptability in the face of model uncertainties and unknown disturbances. Unlike the Kalman filter, which relies on precise statistical models of the disturbance, the ESO does not require a pre-defined gust model. It innovatively treats unknown external disturbances and model inaccuracies collectively as an extended state for real-time estimation and compensation. Compared to a Luenberger observer, which depends on an accurate linear system model, the ESO exhibits stronger robustness.

Specifically, a nonlinear continuous ESO is designed in this work, grounded in the active disturbance rejection control (ADRC) methodology [44]. The actual flight dynamics involve complex, transient gusts and unmodeled rigid–flexible couplings, which challenge a purely linear observer. The nonlinear ESO provides a critical advantage: its fal($\cdot$) function ensures faster convergence and greater robustness against model mismatches during rapid transients compared to a linear counterpart. This design makes it particularly suitable for the high-performance disturbance estimation required in this work, as supported by its prior success in aerospace applications [45,46]. The ESO can be expressed as

$$\begin{cases} E = Z_1 - q \\ \dot{Z}_1 = Z_2 - \beta_{01}E + A_{21}\alpha_r + A_{22}q + B_{21}\delta e + B_{22}\delta a \\ \dot{Z}_2 = -\beta_{02}\mathrm{fal}(E, \alpha_1, \delta) \end{cases} \tag{20}$$

in which E is an evaluation error of the ESO, Z_1 and Z_2 are the observer outputs, and β_{01} and β_{02} are the observer gains. The parameters β_{01} and β_{02} are systematically designed based on the observer bandwidth concept. For a second-order ESO designed for a first-order system in Equation (20), the characteristic equation of its error dynamics is $s^2 + \beta_{01}s + \beta_{02} = 0$. Placing both poles at $-\omega_0$ to achieve a desired bandwidth, ω_0, yields the parameterization

$\beta_{01} \approx 2\omega_0$, $\beta_{02} \approx {\omega_0}^2$. The bandwidth must be substantially higher than the dominant disturbance frequency. Given the aircraft's short-period mode frequency of 0.994 Hz, the target observer bandwidth $f_{BW} = \omega_0/(2\pi)$ is set to 10–15 Hz ($\omega_0 \approx$ 60–90 rad/s). Initial gains derived from ω_0 = 90 rad/s (β_{01} = 180, β_{02} = 8100) are refined through simulation on the rigid–flexible coupling model to balance convergence speed with noise sensitivity and robustness to model uncertainties. This is achieved by evaluating the root mean square error of the AoA estimation to quantify convergence performance, while simultaneously injecting noise into the pitch rate measurement to assess the resultant fluctuations in the estimated α_g and thus gauge noise sensitivity. Furthermore, robustness is tested by varying key aerodynamic derivatives and monitoring the stability and accuracy of the estimation. Through parameter sweeps and a trade-off analysis of these criteria, the final values, β_{01} = 100 and β_{02} = 7000, are selected.

The nonlinear function, fal(·), in Equation (20) is defined as [44]

$$\text{fal}(E, \alpha_1, \delta) = \begin{cases} |E|^{\alpha_1} sign(E), & |E| > \delta \\ E/\delta^{1-\alpha_1}, & \text{otherwise} \end{cases} \tag{21}$$

where $0 < \alpha_1 < 1$, $\delta > 0$. The function operates in two regimes to enhance performance: for large errors ($|E| > \delta$), the term $|E|^{\alpha_1} sign(E)$ provides superlinear convergence, enabling rapid rejection of significant disturbances. For small errors ($|E| \leq \delta$), it switches to a linear gain, $E/\delta^{1-\alpha_1}$, which mitigates high-frequency chattering and improves noise immunity near equilibrium. The choice of parameters α_1 = 0.5 and δ = 0.05 is the result of a simulation-based trade-off study, as mentioned before, seeking an effective balance between aggressive disturbance estimation and smooth observer output. For appropriate values of β_{01}, β_{02}, α_1, and δ, the observer output, Z_1, approaches the angular velocity, and Z_2 approaches the angular acceleration.

The part of angular acceleration that is contributed by measured flight conditions and control input has already been included in the second equation of Equation (20). The rest of the equation, which is $(Z_2 - \beta_{01}E)$, represents the portion of the angular speed that is contributed by gusts. According to Equation (19), α_g can be estimated by

$$\alpha_g = (Z_2 - \beta_{01}E)/A_{21} \tag{22}$$

3. Gust Response and Flight Performance for Validation

3.1. The Aircraft and Gust Models

Different from designing LQR controllers based on reduced-order linear dynamic models, simulation models are executed with a nonlinear time-domain solver that retains large-angle kinematics, updates both quasi-steady and unsteady aerodynamic forces at every time step, and couples elastic deflection with rigid-body motion.

All dynamic simulations in this study commence from a pre-computed static aeroelastic trim condition, determined through the iterative process detailed in Figure 7. This pre-analysis provided the equilibrium parameters: a tail-plane deflection of -10°, an AoA of 7°, and the corresponding stabilized structural deflections.

In the time-domain simulation, the model is initialized from 0 s to 1 s with trimmed tail-plane deflection, AoA at a cruise speed of 10 m/s, and an altitude of 50 m as the trim condition without any external disturbances. During this brief numerical stabilization phase, the flexible wing naturally converges to its pre-computed trimmed structural deflections, thereby establishing a fully consistent aeroelastic equilibrium state in the dynamic environment. After this initialization period, gust disturbances or maneuver commands are applied. Consequently, all subsequent system responses are guaranteed to originate from a verified and stable trim condition.

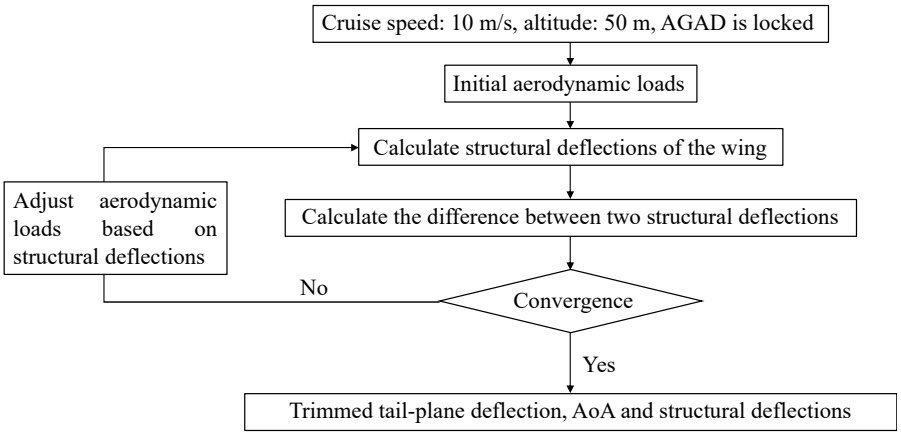


Figure 7. Static aeroelastic iteration process.

A small aircraft model of conventional configuration, as illustrated in Figure 8, is taken in the current case study, and the specific parameters of this aircraft are provided in Appendix A.4. The maximum take-off mass of the aircraft is 3 kg with a designed cruise speed of 10 m/s, which is much lower than the critical flutter speed of 24.5 m/s, as shown in Appendix A.1/Table A2. The wing semi-span is 1 m, and the structure is modeled by using five segment beams, including four flexible wing segments, with the fifth as the AGAD rigid-body segment at the wingtip. The wing has a thin and curved airfoil section so that the structure's bending stiffness is much greater than the torsion stiffness, as presented in Figure 8. For the baseline aircraft design, the AGAD is locked to form one continuous wing surface from root to tip. When the AGAD is unlocked and driven by the controller, the rest of the aircraft data remains the same as the baseline.

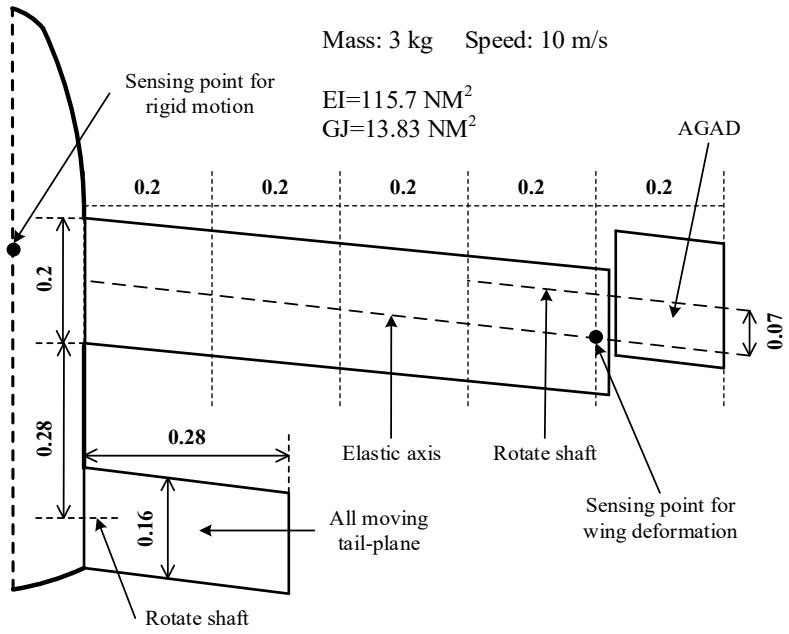


Figure 8. Configurations of the aircraft with the AGAD (unit: m).

The differences in the control system between the baseline aircraft and the aircraft with AGAD unlocked are shown in Table 1. The control commands for the tail-plane and AGAD are calculated based on Equations (7)–(9). Both the baseline aircraft and the aircraft with AGAD unlocked have the same control law for the tail-plane. The difference between the two cases is the active control of the AGAD.

Table 1. Control differences between baseline case and AGAD case.

Categories	Baseline Case	AGAD Case
Optimal control inputs	$u^*(t) = -Q_2^{-1}B^TPx(t) + Q_2^{-1}B^Tg(t)$	
System state $x(t)$	$x(t) = [\alpha(t) \quad q(t) \quad \theta(t)]^T$	
Tracking signal $g(t)$	$g(t) = [\alpha_E(t) \quad q_E(t) \quad \theta_E(t)]^T$	
Control inputs $u^*(t)$	$u^*(t) = u(\delta e)$	$u^*(t) = [u(\delta e) \quad u(\delta a)]^T$
Feedback gain matrix ($-Q_2{}^{-1}B^TP$)	$[-0.028 \quad 0.771 \quad 0.998]$	$\begin{bmatrix} -0.028 & 0.771 & 0.998 \\ -1.688 & 0.0025 & 0.1964 \end{bmatrix}$
Tracking gain matrix ($Q_2{}^{-1}B^T$)	$[0 \quad -0.383 \quad 0]$	$\begin{bmatrix} 0 & -0.383 & 0 \\ 0.034 & 0 & 0 \end{bmatrix}$
Feedback relation for tail-plane	$u(\delta e) = [-0.028 \quad 0.771 \quad 0.998]x(t) + [0 \quad -0.383 \quad 0]g(t)$	
Feedback relation for AGAD	-	$u(\delta a) = [-1.688 \quad 0.0025 \quad 0.1964]x(t) + [0.034 \quad 0 \quad 0]g(t)$

Specifically, the design of the LQR controller hinges on the appropriate selection of weighting matrices Q_1 and Q_2 in Equation (5). Matrix Q_1 is structured to heavily penalize deviations in AoA and pitch angle, as suppressing these states is central to both gust alleviation and maneuver tracking. The control weighting matrix Q_2 is tuned to realize a desired control allocation strategy: the tail is primarily responsible for pitch stabilization, while the AGAD is predominantly utilized to adjust AoA to counteract gusts, thereby preventing actuator saturation and ensuring practical implementability. To grant the AGAD greater authority in generating control moments for AoA adjustment, its control effort is penalized less in the Q_2 matrix compared to that of the tail. On this basis, the Riccati equation (Equation (8)) is used to solve for the feedback gain and tracking gain in cruise speed of 10 m/s.

In this study, a (1 − cos) gust model, as expressed below, is taken for vertical gust velocity input:

$$U_g = \frac{V_{ds}}{2}\left[1 - cos(\omega_g t)\right] \tag{23}$$

where V_{ds} is a specified gust velocity variation in magnitude (V_{ds} = +/−5 m/s) and frequency (1 Hz) as illustrated in Figure 9 in this case study; $\omega_g = \pi s/(tH)$ is the gust frequency, in which $s = Vt$ is the penetrating distance of an aircraft at an equivalent flight speed, V, into a discrete gust at time t. H is the half-gust gradient distance.

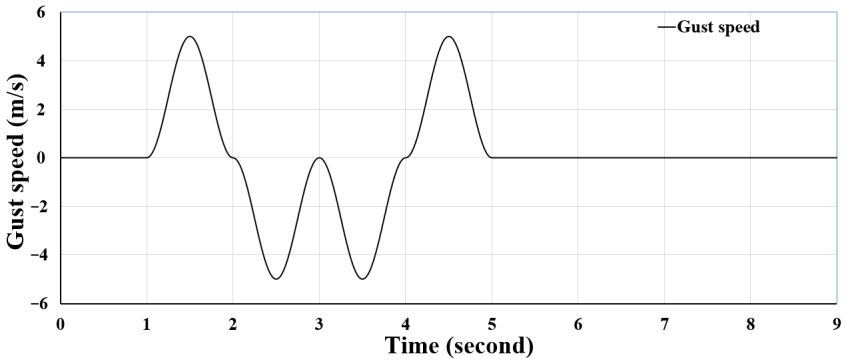


Figure 9. Gust speed during the dynamic response.

As illustrated in Figure 8, the sensing points are located at the CG of the aircraft and the end of the flexible inner wing (segment 4). Since the sensors only measure rigid-body motion and wing deformation, the AoA of the aircraft is estimated based on the ESO expressed in Equations (19)–(22). Taking the baseline case using tail-plane control alone, for example, the estimated AoAs of the aircraft in response to the gust are shown in Figure 10. The AoA values in Figure 10 represent variations relative to a trimmed AoA of 7° under gusts. The primary purpose of this figure is to validate the capability of the ESO, as a

disturbance observer, to accurately estimate the unmeasurable GAoA, which is a key state variable in the closed-loop control system.

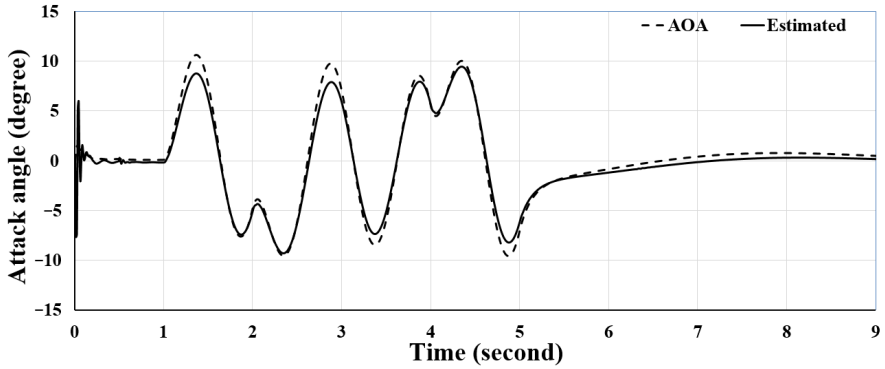


Figure 10. The estimated AoA deviation from the actual result in response to the gust.

Figure 10 shows that, except for brief peak moments when the aircraft attitude deviates sharply from the trimmed condition, the estimation error of the ESO is negligible. This confirms the effectiveness of the ESO design: its nonlinear fal(·) function enables fast convergence and robust tracking of the rapidly varying equivalent AoA disturbance caused by gusts.

Notably, the simulation presents a demanding scenario: a 5 m/s vertical gust at a cruise speed of 10 m/s can theoretically induce an instantaneous AoA disturbance of up to 30°, posing a significant stall risk. However, as shown in Figure 10, the maximum AoA deviation in the baseline case (with the AGAD locked and tail-plane-only control) is limited to about 10°. This substantial attenuation fundamentally relies on the accurate estimation of the AoA state provided by the ESO to the LQR. Based on this estimate, the LQR controller can generate real-time counteracting commands and coordinate tail-plane deflection, thereby preventing the aircraft from approaching the theoretical stall-critical AoA. Therefore, Figure 10 not only demonstrates the control performance but also, from the perspective of state estimation, verifies the feasibility of the LQR-ESO framework in handling external aerodynamic disturbances. It establishes a reliable state-feedback foundation for the subsequent integration of the AGAD and the coordinated optimization of multiple control surfaces.

3.2. The Gust Response and Flight Attitude Results

3.2.1. Rigid-Body Motion

The rigid-body motion responses in terms of the pitch and heave motion of the aircraft due to gusts for the baseline case (AGAD-locked) and the case with the AGAD in operation are shown in Figure 11. The primary purpose of this figure is to quantitatively evaluate the effectiveness of the presented AGAD control framework from the dual perspectives of flight quality and disturbance rejection.

The results show that with the AGAD, the aircraft flight attitude has been significantly improved. The peak values of the pitch angle, normal acceleration, and heaving motion are reduced by 57.46%, 20.28%, and 21.99%, respectively. This improvement stems from the unique role of the AGAD as an additional control surface at the wingtip: it can directly and rapidly alter the aerodynamic force distribution on the outer wing section, thereby generating compensating moments and forces opposite to the gust disturbance. This synergistic action with the tail-plane achieves more efficient damping of pitch, normal motion, and heave displacement, resulting in less overshoot and an overall smoother aircraft response.

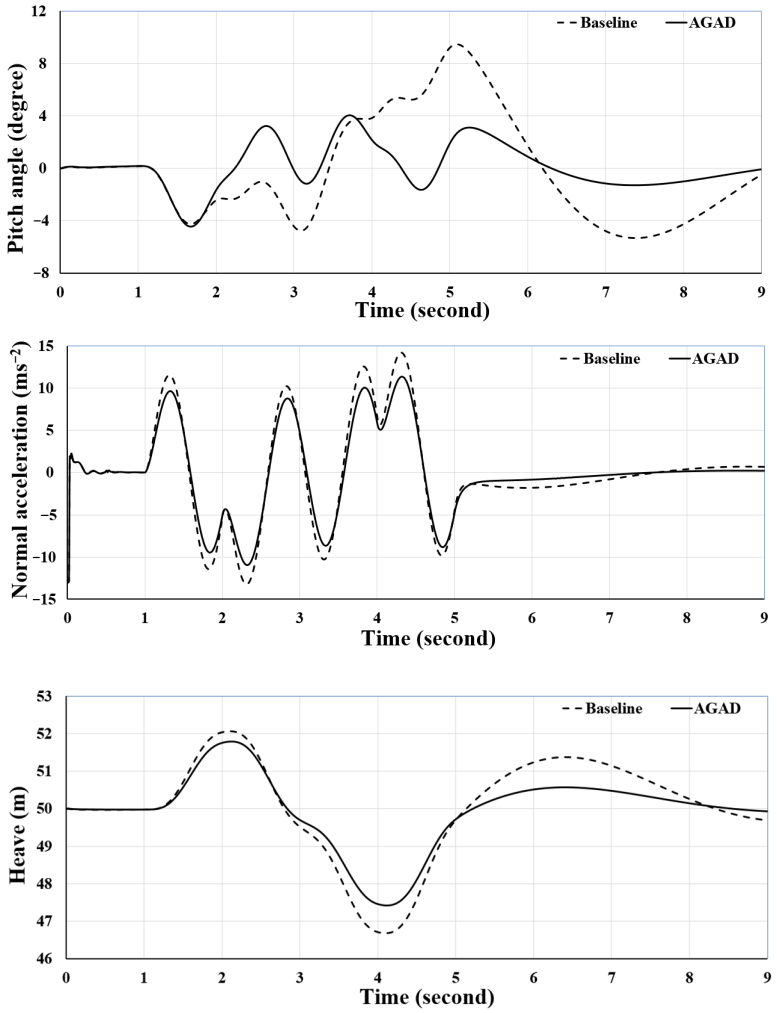


Figure 11. Aircraft rigid body motion under gust in the baseline and AGAD control.

To further quantify the improvement in the dynamic convergence quality of the system, we introduce the integral of time-weighted absolute error (ITAE). This metric penalizes persistent errors more heavily over time, thus providing a measure of both response speed and settling performance. It can be expressed as

$$ITAE = \int_0^T t \cdot |e(t)| dt \tag{24}$$

where $e(t)$ represents the error between the desired value and the actual value. Since the goal is to quickly return the aircraft to its initial trim state, the desired value of pitch angle and normal acceleration are 0° and 0 m/s^2, respectively.

The ITAE values for the pitch angle and normal acceleration are significantly lower with AGAD control than with the baseline control. Specifically, the ITAE of the pitch angle is reduced by 66.87%, and that of the normal acceleration is reduced by 19.25%. This carries dual significance: First, it confirms that the controller not only reduces instantaneous overshoot but fundamentally accelerates the system's recovery to equilibrium, enhancing transient response speed. Second, lower ITAE values indicate a smaller cumulative deviation from the desired state over the entire disturbance period, which is directly linked to more stable flight trajectories, higher mission reliability, and improved comfort for occupants or sensitive payloads. The detailed data is shown in Table 2.

Table 2. Rigid-body motion performance between baseline case and AGAD case.

Performance Indicators	Baseline	AGAD	Improvement
Pitch angle peak (°)	9.45	4.02	−57.46%
ITAE of pitch angle (°·s)	154.20	51.09	−66.87%
Normal acceleration peak (m·s^{-2})	14.15	11.28	−20.28%
ITAE of normal acceleration (m·s^{-1})	119.13	96.20	−19.25%
Heave displacement peak (m)	−3.32	−2.59	−21.99%

Therefore, Figure 11 provides compelling evidence at the rigid-body motion level, demonstrating that the proposed AGAD system is not merely an added control surface. Instead, through its deep integration with the tail-plane via optimal control laws, it significantly enhances the aircraft's stability, control precision, and mission adaptability in turbulent environments.

3.2.2. Control Outputs

An analysis is carried out to evaluate the effectiveness of the baseline case and the AGAD case in operation. The AGAD contributes to the aerodynamic force on the wing directly and is a dominant factor in normal acceleration due to its gust response. The tail-plane plays a dominant role in the pitching moment and is set at an initial angle of −10° to trim the aircraft. Its variation influences the aerodynamic force on the wing indirectly through the change in attitude in terms of pitch angle or the AoA. The resulting rotations of the tail-plane and AGAD are shown in Figure 12. The primary purpose of this figure is to reveal the practical implementation of the proposed control allocation strategy and to evaluate the role of the AGAD in sharing the control burden and optimizing actuator operation.

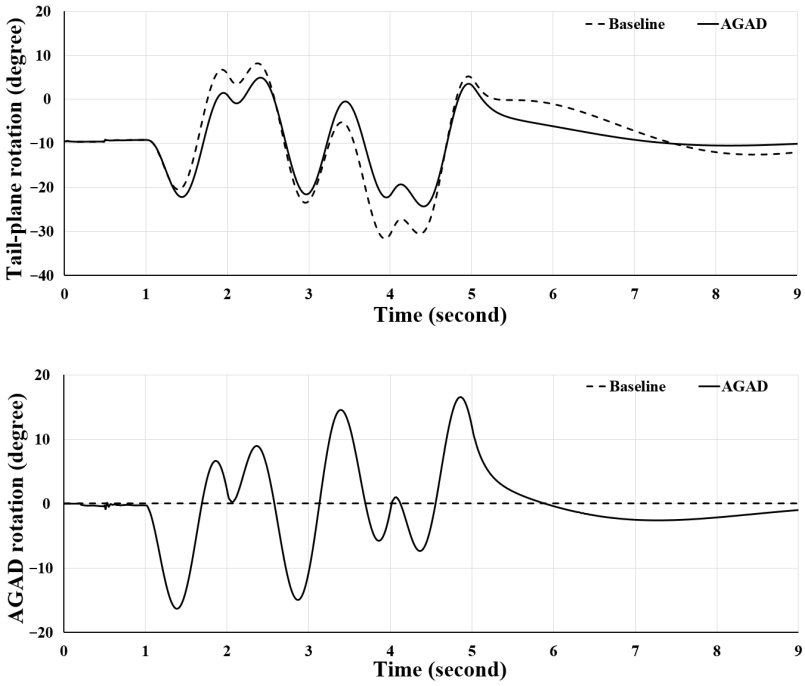


Figure 12. Control outputs of tail-plane and AGAD in the baseline and the AGAD control.

For the baseline case, the tail-plane deflection reaches a peak of −31.61°, as shown in Figure 12. It is worth noting that even if the deflection angle is large, the simulation result shows that the tail AoA is controlled within a bounded range of ±10° and will not cause tail stall problems. In contrast, with the AGAD engaged, the peak tail-plane

deflection is reduced to −24.32°, a reduction of 23.06%. This change visually demonstrates the inherent logic of the control allocation: through the tuning of the weighting matrix in the LQR controller, the AGAD is granted greater authority to generate control commands that directly counteract the aerodynamic moments induced by gusts. Consequently, this partially relieves the tail-plane from the demanding task of pitch stabilization, allowing it to operate within a more efficient and safer deflection range. It should be noted that the tail-plane deflection in Figure 12 starts from −10°. This is the initial setting at the trim condition for the flexible-wing aircraft, as we mentioned before, stemming from its unique aerodynamic characteristics.

To further evaluate the control effort throughout the entire gust encounter, we introduce root mean square (RMS) as a metric to quantify the overall intensity of the tail-plane rotation as

$$RMS = \sqrt{\frac{1}{n}\sum_{i=1}^{n} {x_i}^2} \tag{25}$$

where x_i represents discrete data points of the control signal.

The RMS value for the tail-plane rotation is reduced by 14.41%. This signifies not merely a reduction in peak load but indicates a systematic decrease in the average actuation intensity and energy consumption of the tail-plane throughout the entire disturbance response. This overall reduction in control activity directly translates to lower servo energy consumption, reduced heat generation, and significantly decreased actuator wear, offering substantial practical engineering value for extending the flight endurance and maintenance intervals of the aircraft.

Therefore, Figure 12 provides evidence from the actuator level of the dual benefits brought by AGAD integration: it not only enhances transient disturbance rejection through control allocation but also improves the long-term operational economy and reliability of the system by reducing actuation loads.

The maximum rotation angle demanded of the auxiliary AGAD is 16.32°. As shown in Figure 12, the variations in both the tail-plane and AGAD rotation angles remain within a reasonable range, confirming the practical feasibility of the proposed control strategy. The detailed data is shown in Table 3.

Table 3. Control outputs between baseline case and AGAD case.

Performance Indicators	Baseline	AGAD	Improvement
Tail-plane rotation peak (°)	−31.61	−24.32	−23.06%
Tail-plane rotation RMS (°)	13.67	11.70	−14.41%
AGAD rotation angle (°)	-	16.32	-

3.2.3. Elastic Deformation of the Flexible Wing

The elastic deformation of the flexible wing is also discussed in this section. The variation in wingtip twist angle and wingtip bending deflection is depicted in Figure 13. The purpose of this figure is to elucidate the underlying aeroelastic mechanism through which the AGAD achieves gust alleviation, moving beyond rigid-body control to actively shape structural responses for improved load management.

The AGAD controller alleviates gusts by actively altering the wing's aerodynamic force distribution, harnessing a beneficial aeroelastic effect. This strategy is evidenced by the distinct deformation patterns in Figure 13. Specifically, the AGAD induces a significantly larger wingtip twist angle (a peak of 1.92° compared to 1.5° in the baseline) while simultaneously reducing the wingtip bending deflection (from 0.041 m to 0.029 m). This combination is not incidental; the increased twist is a direct result of the AGAD's commanded rotation, which deliberately induces torsional deformation to redistribute aero-

dynamic loads. The reduction in bending deflection indicates a more favorable load path and lower structural stresses. This combination of increased twist and reduced bending indicates a more favorable load distribution that enhances gust alleviation.

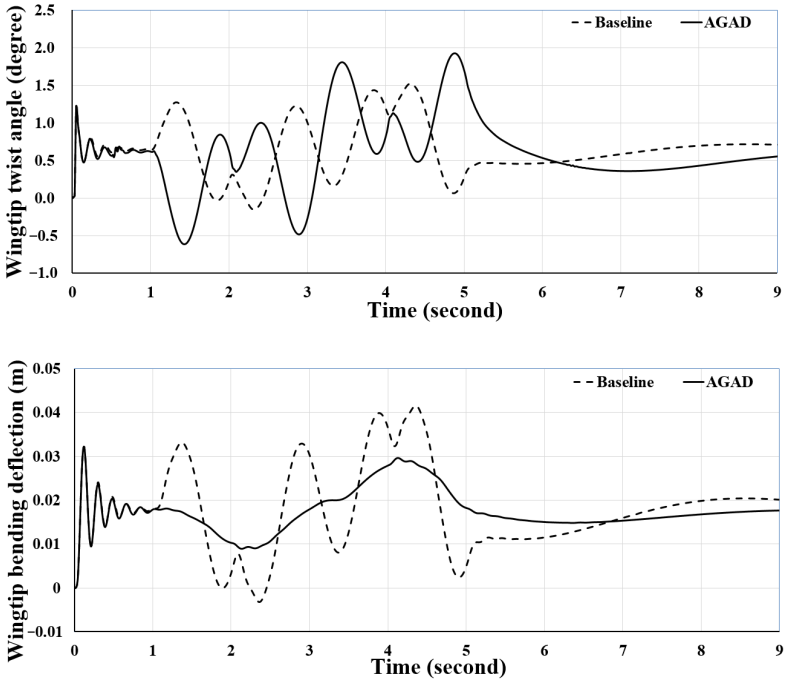


Figure 13. Elastic deformation of the flexible wing in the baseline and the AGAD control.

Crucially, as seen in Figure 13, the wing twist under AGAD control is approximately 180 degrees out of phase with the passive, tail-dominated response of the baseline. This phase reversal demonstrates that the AGAD generates counteracting aerodynamic forces that are not only different in magnitude but also opposite in their dynamic action compared to the baseline case. The detailed data is shown in Table 4.

Table 4. Elastic deformation between baseline case and AGAD case.

Performance Indicators	Baseline	AGAD	Improvement
Wingtip twist angle peak (°)	1.5	1.92	28%
Wingtip bending deflection peak (m)	0.041	0.029	−29.27%

Thus, Figure 13 contributes fundamentally to the overall understanding of the work by validating that the AGAD functions not just as an additional control surface but as an integrated element in a controlled aeroelastic system. It visually confirms the strategy of using intentional, active twists to mitigate gust loads—a principle that enhances both immediate flight stability and long-term structural durability.

3.2.4. Variation in Physical Quantities at Wing Root

In addition to improving the aircraft's flight stability, AGAD has also significantly reduced the gust load on the wing structure. The resulting bending moment (BM), shear force (SF), and torque calculated at the wing root are presented in Figure 14.

The results confirm that AGAD control is more effective in reducing structural loads compared to the baseline using tail-plane control only. A key observation is the significant reduction in peak loads, with the bending moment, shear force, and torque decreasing by 20.87%, 15.22%, and 14.69%, respectively. This indicates a substantial enhancement

in the wing's ability to withstand extreme gust events. Furthermore, the reductions in RMS values—by 9.43% for bending moment, 7.96% for shear force, and 5.71% for torque—demonstrate a consistent attenuation of dynamic load fluctuations. This lowering of the average load cycle is critical for extending the structural fatigue life of the flexible wing, thereby significantly improving its long-term structural safety. The detailed data is shown in Table 5.

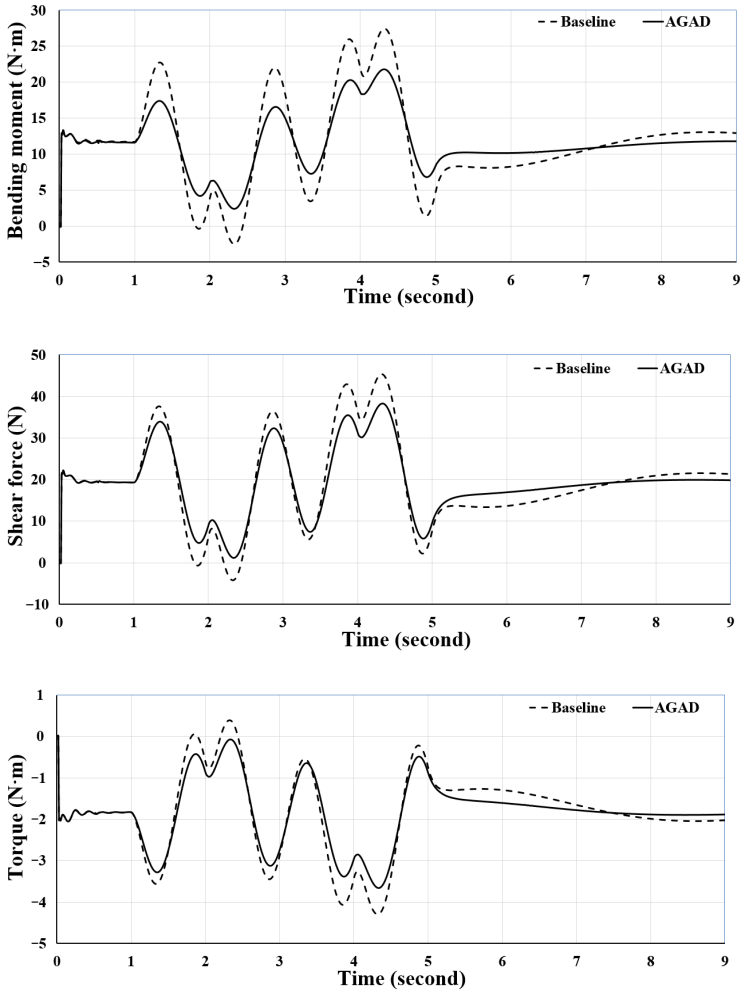


Figure 14. The BM, SF, and torque at the wing root with and without the AGAD control.

Table 5. Variation in physical quantities at wing root between baseline case and AGAD case.

Performance Indicators	Baseline	AGAD	Improvement
Bending moment peak (N·m)	27.45	21.72	−20.87%
Bending moment RMS (N·m)	13.26	12.01	−9.43%
Shear force peak (N)	45.13	38.26	−15.22%
Shear force RMS (N)	22.25	20.48	−7.96%
Torque peak (N·m)	−4.29	−3.66	−14.69%
Torque RMS (N·m)	2.10	1.98	−5.71%

3.3. Maneuvering Performance of the Aircraft with the AGAD

A study has also been carried out on the enhancement of aircraft maneuverability using baseline control and AGAD control. In this case, the aircraft is initially trimmed for a level flight with 50 m altitude at cruise speed without gusts and needs to climb an additional 7 m in altitude. The flight attitude and wingtip twist of the aircraft under baseline control and AGAD control are shown in Figure 15.

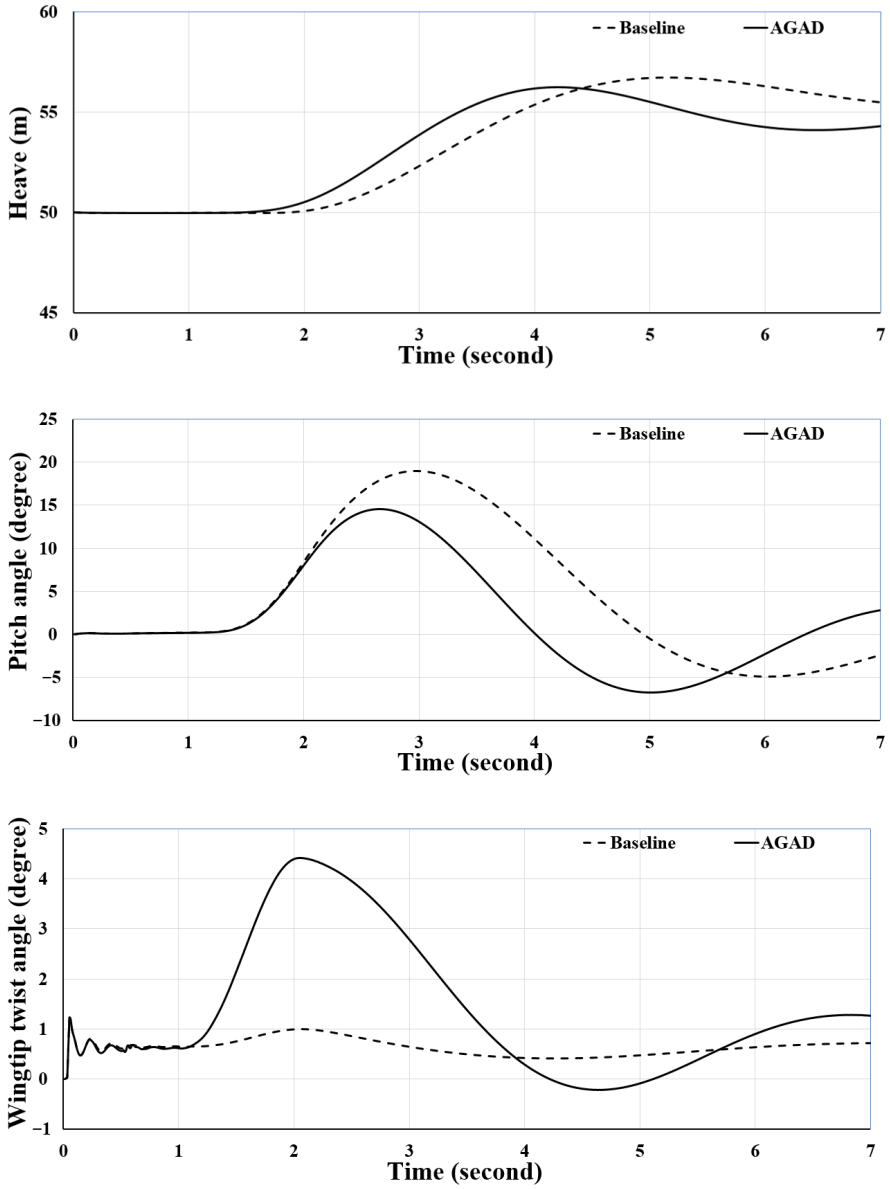


Figure 15. Flight attitude and wing twist of the aircraft with and without the AGAD.

The optimal control of the tail-plane for the baseline control achieved the target within 5 s, as shown in Figure 15. The maneuver action is finished within 4 s at a greater climbing rate and a smaller pitch angle with AGAD control, and the pitch angle is decreased by 23.74%. Such an improvement in flight performance is due to the wing lift increase caused by operating the AGAD like an aileron. For the same reason, the wing elastic twist angle due to the AGAD control is much larger than that of the baseline wing. It should be noted that the classic non-minimum phase undershoot is suppressed by the inherent passive aeroelasticity of the flexible wing. This suppression occurs because the aeroelasticity introduces a novel pathway distinct from rigid-body aircraft: a maneuver command concurrently generates a rigid-body rotation and a favorable, instantaneous wing twist that acts to counteract the initial lift transient. The pole trajectories of the system matrix in Figure 16 also demonstrate that within the maneuver envelope, the system matrix always has negative real parts, which shows that the flexible-wing aircraft is stable during the maneuver progress.

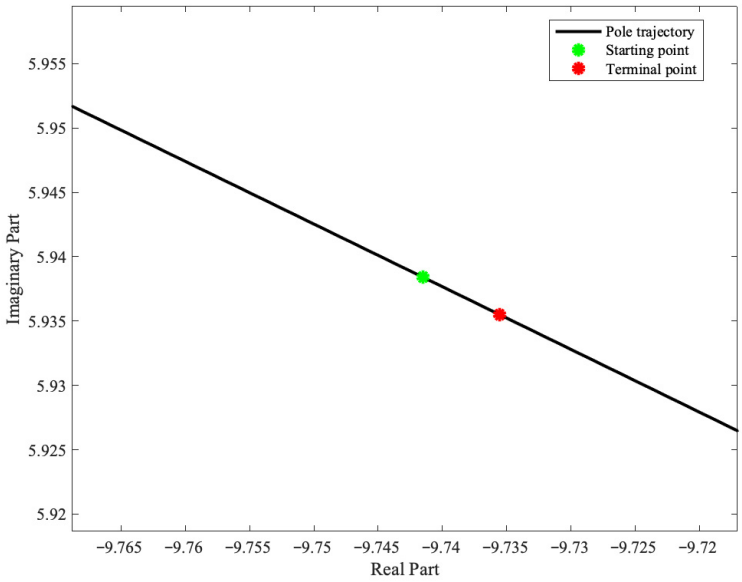


Figure 16. Pole trajectories of system matrix during maneuvering.

4. Discussion

In recent years, small flexible-wing aircraft have undergone rapid development for urban applications due to their flexibility and maneuverability. However, their operation at low Reynolds numbers makes them susceptible to gust disturbances, posing significant challenges to flight stability.

To address this problem, gust alleviation strategies have been explored. Passive techniques utilize anisotropic composite materials, while active methods employ control surfaces. Although it is simpler to implement, passive alleviation is generally less effective than its active counterpart. In this study, we propose a hybrid approach by designing an AGAD attached to the wingtip to work in concert with the conventional tail-plane for enhanced flight attitude control.

Our research mainly focuses on vertical gust disturbances—the primary threat to small, low-inertia aircraft due to rapid changes in the effective AoA. Consequently, an integrated longitudinal aircraft dynamics model was presented using the residualized model method, incorporating aeroelastic effects. Given the multi-variable control nature of this system, an LQR scheme was adopted. An ESO was utilized to estimate the complete AoA under gust conditions, which comprises the RAoA and gust-induced GAoA.

The effectiveness of the AGAD was validated through simulations of a small flexible-wing aircraft. Two configurations were compared: a baseline case with tail-plane control only and an AGAD case with unified AGAD and tail-plane control. Evaluations included gust response and maneuver performance without gusts.

The gust response simulations demonstrated that the AGAD configuration significantly improved performance with lower control effort. Specifically, compared to the baseline, the AGAD case reduced pitch angle peak by 57.46%, normal acceleration peak by 20.28%, and heave displacement peak by 21.99%, indicating substantially improved flight stability. Notably, while the wingtip twist angle peak increased by 28% (reflecting a more effective gust alleviation ability), the structural loads were markedly reduced: wingtip bending deflection peak decreased by 29.27%, wingroot bending moment peak by 20.87%, wingroot shear force peak by 15.22%, and wingroot torque peak by 14.69%. This suggests that the AGAD not only suppresses gust effects but also enhances structural safety by redistributing and alleviating air loads. Furthermore, the required tail-plane rotation angle peak was reduced by 23.06%, implying savings in control effort.

In maneuver simulations, the aircraft equipped with AGAD exhibited greater agility. It reached a specified altitude 1 s faster than the baseline, with a 23.74% reduction in pitch angle peak. This enhanced maneuverability is attributed to the ability of AGAD to generate rapid and large-amplitude wingtip twist responses, providing additional pitch control power.

While the simulations demonstrate significant performance improvements under the designed cruise condition and a standard (1 − cos) gust, the robustness of the proposed AGAD control strategy to operational uncertainties is a critical aspect for practical deployment. The robustness of the proposed control strategy can be evaluated by examining the fundamental assumptions of its underlying model. Firstly, the reduced-order model's validity is contingent upon the aircraft operating sufficiently below the flutter speed. Within this flight envelope, the model intrinsically captures the effects of varying speed and altitude through the aerodynamic derivatives. Secondly, the ESO does not rely on a pre-defined gust model. Its fal(·) function is designed for rapid estimation of aggregated disturbances, granting the controller inherent adaptability to diverse gust profiles, including non-periodic ones like clear air turbulence. Finally, the core premise of the model reduction is the frequency separation between rigid-body and elastic dynamics. The control framework remains applicable as long as this separation is preserved under variations in wing stiffness, defining a clear and practical robustness threshold. To evaluate its robustness, AGAD control is tested in Appendix A.5 under varying gust amplitudes and shapes. The results remained consistent with those in the main text, demonstrating a reduction in pitch angle and an increase in wingtip twist angle compared to the baseline, thereby illustrating the robustness of the control strategy.

It is also important to address the system-level implications of integrating AGAD. Our study focuses on longitudinal gust alleviation, where the two AGADs mounted on the wingtips are operated symmetrically to counteract vertical gusts. In this symmetric mode, the AGAD has a minimal impact on lateral control authority. Furthermore, the auxiliary AGAD adds weight and drag. The AGAD mechanism adds approximately 0.1 kg to the aircraft, which is marginal relative to the total mass of 3 kg. Similarly, the AGAD panel area of 0.04 m^2 is small compared to the total wing area of 0.4 m^2, suggesting a manageable impact on overall drag. While these penalties are non-negligible, they are decisively outweighed by the fundamental improvements in flight safety and gust alleviation capability—a critical enhancement for reliable operation in complex, low-altitude missions such as environmental monitoring and disaster response.

Beyond the weight and drag considerations, the practical feasibility of the proposed AGAD control system is a key consideration. The control commands generated by the LQR controller, with a maximum absolute deflection of approximately 24° for the tail-plane and 16° for the AGAD, fall well within the typical mechanical range of standard small UAV servos. Furthermore, the control system only needs to respond to low-frequency dynamics dominated by the aircraft's short-period mode (0.994 Hz). The resulting bandwidth requirement is modest and well within the performance envelope of common servo actuators. Regarding the concern of sensor noise, it is important to note that the employed nonlinear ESO itself possesses inherent noise-suppression capabilities, which are factored into its fal(·) design, allowing the ESO to differentiate between noisy signals and true disturbances. Therefore, although the current validation is simulation-based, the proposed control system's demands on actuation and sensing align well with the capabilities of commercially available components, supporting its feasibility for future physical implementation.

To further illustrate the contribution of this work, the proposed AGAD is contrasted with active multi-flap systems from the literature, such as the work by Berg et al. [27], as well as with the actively controlled FFWT system studied by Narimani et al. [32]. The

multi-flap system, employing six independently actuated trailing-edge flaps, represents a high-performance yet high-complexity approach to load alleviation, requiring intricate actuation coordination, high-fidelity aeroelastic modeling, and multi-sensor fusion. Similarly, the FFWT system utilizes a linear model predictive control strategy combined with unsteady aerodynamic modeling based on Theodorsen's theory, which, while effective in gust load alleviation and limit-cycle oscillation suppression, demands significant computational resources and accurate disturbance prediction. In contrast, as summarized in Table 6, the AGAD scheme adopts an intentionally simplified design suitable for resource-constrained platforms. It utilizes a single wingtip control surface on one side of the wing instead of a complex multi-flap or morphing wingtip system, prioritizing flight stability and primary structural load control for small flexible aircraft. The comparison demonstrates that the AGAD achieves gust alleviation performance comparable to both the multi-flap and FFWT systems in key metrics, despite a drastic reduction in system complexity. Consequently, this work establishes that the AGAD presents a practical alternative for small UAVs, offering a favorable trade-off between performance and complexity for cost- and weight-sensitive applications.

Table 6. Comparison between the AGAD and a multi-flap system.

Comparison Metric	Multi-Flap System ([27])	FFWT-LMPC System ([32])	AGAD System
Actuator count (one side of the wing)	6	1	1
Gust alleviation performance ((1 − cos) gust)	Wingtip acceleration reduction: 30%	Wing root bending moment reduction: nearly 11%	(a) Wingtip bending deflection reduction: 29.27%; (b) Wing root bending moment reduction: 20.87%
System complexity	High	High	Low

In future work, we will explore the integration of recent advancements in morphing wing technology based on the AGAD concept. This may involve incorporating additional control surfaces and diverse control modes, including differential AGAD actuation for roll control to further improve the stability, maneuverability, and agility of flexible-wing aircraft, ultimately enabling safer and more reliable operations in complex urban environments and expanding their potential applications.

5. Conclusions

This study proposes an integrated strategy based on an AGAD and an LQR-ESO control framework to enhance the flight stability and maneuverability of small flexible-wing aircraft in gust environments. By establishing a reduced-order model that considers aeroelastic effects and designing an ESO to estimate the GAoA in real time, optimal coordinated control between the AGAD and the all-movable tail-plane is achieved.

The simulation results demonstrate that, compared to the baseline case using tail-plane control alone, the proposed AGAD strategy achieves significant improvements in multiple aspects. In the study of flight stability under gusts, at the rigid-body motion level, the peak pitch angle, normal acceleration, and heave displacement are reduced by 57.46%, 20.28%, and 21.99%, respectively; at the structural load level, the peak wing root bending moment, shear force, and torque are reduced by 20.87%, 15.22%, and 14.69%, respectively; at the control efficiency level, the peak tail-plane deflection angle is reduced by 23.06% and the RMS index by 14.41%. Furthermore, by inducing a 28% increase in wingtip twist angle, the AGAD reduces the peak wingtip bending deflection by 29.27%, achieving a more favorable aerodynamic load distribution, which further verifies its mechanism of enhancing

gust alleviation capability through aeroelastic coupling. In the study of maneuverability, utilizing the AGAD reduces the time to complete a specified climbing task by 1 s and lowers the peak pitch angle by 23.74%.

This study not only confirms the effectiveness of the AGAD in gust control for small flexible aircraft but also provides a practical solution that balances performance and complexity for resource-constrained platforms. Future work will explore the integration of AGAD with roll control and its further application in complex urban environments.

Author Contributions: Conceptualization, Y.W. and Y.F.; Data Curation, Y.F.; Formal Analysis, Y.W., Y.F., H.L., X.L. and H.S.; Funding Acquisition, Y.W.; Investigation, Y.F.; Methodology, Y.W. and Y.F.; Project Administration, Y.W.; Resources, Y.W.; Software, Y.F.; Supervision, Y.W.; Validation, H.L., X.L. and H.S.; Visualization, Y.F.; Writing—Original Draft, Y.F.; Writing—Review and Editing, Y.W. and Y.F. All authors have read and agreed to the published version of the manuscript.

Funding: This research was funded by the Chinese Natural Science Funding Council (NSFC 11672033) and the Key R&D Program of Shandong Province (2015GGE27226) for financial support of the project.

Data Availability Statement: The original contributions presented in this study are included in the article. Further inquiries can be directed to the corresponding author.

Acknowledgments: We are thankful for the thorough review and valuable feedback provided by the anonymous reviewers.

Conflicts of Interest: The authors declare no conflicts of interest.

Abbreviations

The following abbreviations are used in this manuscript:

ACFWT	Active controlled folding wingtip
ADRC	Active disturbance rejection control
AGAD	Active gust alleviation device
AoA	Angle of attack
BFF	Body freedom flutter
BM	Bending moment
CFA	Coupled flight dynamics and aeroelasticity model
CG	Center of gravity
ESO	Extended state observer
FFWT	Flared folding wingtip
GAoA	Gust-induced angle of attack
IMU	Inertial measurement unit
ITAE	Integral of time-weighted absolute error
LFW	Large flexible wing
LQR	Linear–quadratic regulator
MPC	Model predictive control
PGAD	Passive gust alleviation device
RAoA	Rigid-body motion angle of attack
RMS	Root mean square
SF	Shear force
VCCTE	Variable camber continuous trailing edge
WRBM	Wing root bending moment

Nomenclature

A	System matrix of the reduced-order model
A_{EE}	State matrix for structural elastic deflection
A_{ER}	Coupling state matrix from rigid-body motion to elastic deflection

a_h	Specified climb acceleration
A_{RE}	Coupling state matrix from elastic deflection to rigid-body motion
A_{RR}	State matrix for aircraft rigid-body motion
B	Input matrix of the reduced-order model
B_{ER}, B_{EE}	Input matrices for structural elastic deflection control
B_{RR}, B_{RE}	Input matrices for rigid-body motion control
$\boldsymbol{e}(t)$	Tracking error vector
J	Cost function
P	Solution of the Riccati equation
q	Pitch angular speed
$\overline{q}$	Dynamic pressure
Q_1	State weighting matrix
Q_2	Control weighting matrix
$\mathbf{u}(t)$	Control input vector
V_h	Vertical velocity in ground global coordinate system
V_x, V_z	Velocity components in local coordinate system
x_E	Structural displacement
$\dot{x}_E$	Structural deformation velocity
x_{EB}	Instantaneous equilibrium deformation
$\widetilde{x}_E$	Residual deformation
$\boldsymbol{x}_R$	State vector of aircraft rigid-body motion
$\boldsymbol{x}_U$	State vector of structural elastic deflection
$\boldsymbol{z}(t)$	Tracking signal vector
α	Angle of attack
α_g	Gust-induced angle of attack (rad)
α_r	Rigid-body motion angle of attack (rad)
δa	Rotation angle for AGAD
δe	Rotation angle for tail-plane
θ	Pitch angle
$(\cdot)^*$	Desired or target value

Appendix A

Appendix A.1. Discussion of Modal Frequency

To accurately obtain the structural dynamics characteristics of flexible wings, we employ ANSYS 2021 R1 for modeling. A finite element model of the flexible membrane wing is constructed based on shell elements to precisely simulate its thin-walled structural characteristics.

At a cruise speed of 10 m/s, the modal frequencies of the flexible wing with a total wing mass of 1 kg can be calculated, as shown in Table A1.

Table A1. Modal frequencies of the flexible-wing aircraft.

Condition	Eigen Value	Low-Order Modal Frequency
Longitudinal short-period mode	$-6.05 \pm 1.54i$	0.994 Hz
Cruise speed of 10 m/s; total wing mass of 1 kg	$-1.19 \pm 35.44i$	5.647 Hz
	$-21.23 \pm 137.29i$	22.121 Hz
	$-63.79 \pm 244.84i$	40.289 Hz
	$-204.05 \pm 399.84i$	71.481 Hz

From Table A1, it can be seen that the frequency of the short-period mode is much lower than the low-order structural modal frequencies of the wing. This result validates the rationality of residual analysis in Equation (3).

To further investigate the aeroelastic safety of the system, we study the dynamic response characteristics of flexible wings that vary with cruise speed, as shown in Table A2.

Table A2. Modal frequencies varying with cruise speed.

Condition	Eigen Value	Low-Order Modal Frequency
10 m/s	$-1.19 \pm 35.44i$	5.647 Hz
	$-21.23 \pm 137.29i$	22.121 Hz
	$-63.79 \pm 244.84i$	40.289 Hz
	$-204.05 \pm 399.84i$	71.481 Hz
20 m/s	$-0.9854 \pm 39.06i$	6.222 Hz
	$-21.49 \pm 113.76i$	18.436 Hz
	$-63.69 \pm 246.33i$	40.515 Hz
	$-204.11 \pm 390.19i$	70.120 Hz
24.5 m/s	$-0.01 \pm 43.91i$	6.992 Hz
	$-22.53 \pm 93.72i$	15.349 Hz
	$-63.56 \pm 247.42i$	40.679 Hz
	$-204.20 \pm 383.59i$	69.197 Hz

From Table A2, it can be seen that as the cruise speed increases, the low-order modal frequencies of the wing undergo significant changes. When the speed reaches 24.5 m/s, the real part of the system's characteristic root is very close to zero and is in a critical flutter state. When the speed increases to 25 m/s, the real part will cross the imaginary axis, and the system will experience flutter.

Appendix A.2. Derivation of Residualization

Deformation of the membrane wing structure (x_E) can be divided into two parts, instantaneous equilibrium deformation of the membrane wing structure (x_{EB}) and residual deformation of the membrane wing structure ($\widetilde{x}_E$), as follows:

$$x_E = x_{EB} + \widetilde{x}_E \tag{A1}$$

The definition of instantaneous equilibrium deformation, x_{EB}, assumes that the membrane wing structure has no inertia, and there is no transitional process in the dynamic response of structural deformation. Under such assumptions, the membrane wing structure always satisfies the condition of static equilibrium with external loads; that is, $\dot{x}_{EB} = \ddot{x}_{EB} = 0$. According to Equation (2), we can obtain

$$\ddot{x}_{EB} = A_{ER-2}x_R + A_{EE-21}x_{EB} + A_{EE-22}\dot{x}_{EB} + [B_{ER}\ B_{EE}]\mathbf{u}(t) \tag{A2}$$

x_{EB}, x_R, and u should satisfy the static equilibrium condition as follows:

$$0 = A_{ER-2}x_R + A_{EE-21}x_{EB} + [B_{ER}\ B_{EE}]\mathbf{u}(t) \tag{A3}$$

Consequently, instantaneous equilibrium deformation, x_{EB}, can be presented as follows:

$$x_{EB} = -{A_{EE-21}}^{-1}A_{ER-2}x_R - {A_{EE-21}}^{-1}[B_{ER}\ B_{EE}]\mathbf{u}(t) \tag{A4}$$

According to Appendix A.1/Table A1, the modal frequencies of composite thin-film membrane wings are significantly higher than the short-period motion frequency of the aircraft. Therefore, the rigid body motion state variable, x_R, which reflects changes in the flight state of the aircraft, belongs to a slow time-varying state variable, and the corresponding instantaneous equilibrium deformation, x_{EB}, is also a slow time-varying state variable. The elastic body motion state variable, x_E, reflecting the deformation motion of the membrane wing structure, belongs to the fast time-varying state variable, and the corresponding residual deformation, $\widetilde{x}_E$, is also a fast time-varying variable.

The rigid body motion part in Equation (2) can be expressed as

$$\begin{aligned}\dot{x}_R &= A_{RR}x_R + A_{RE-1}x_E + [B_{RR}B_{RE}]\mathbf{u}(t)\\ &= A_{RR}x_R + A_{RE-1}\left(x_{EB} + \widetilde{x}_E\right) + [B_{RR}B_{RE}]\mathbf{u}(t)\end{aligned} \tag{A5}$$

Substituting x_{EB}, obtained in Equation (A5), we can then obtain a new linearized dynamic model as follows:

$$\dot{x}_R = A_{RR}x_R + A_{RE-1}\left(-{A_{EE-21}}^{-1}A_{ER-2}x_R - {A_{EE-21}}^{-1}[B_{ER}\ B_{EE}]\mathbf{u}(t) + \widetilde{x}_E\right) + [B_{RR}B_{RE}]\mathbf{u}(t) \tag{A6}$$

Combining the x_R and $\mathbf{u}(t)$ terms like Equation (3), we can then obtain an expression similar to Equation (4).

Appendix A.3. Parameters of the Reduced-Order Dynamic Model

Before presenting the specific calculation equations, we should note that Equation (17) is the expanded form of Equation (3). From Equation (17), it can be observed that in the state-space equation, $\dot{\theta}$ is represented by q. Therefore, we only need to compute the 2×2 matrix of $\begin{pmatrix} A_{11} & A_{12} \\ A_{21} & A_{22} \end{pmatrix}$ in the form of Equation (17).

$$A_{RR} = \begin{pmatrix} \frac{Z_\alpha}{u_0} & 1 \\ M_\alpha + M_{\dot{\alpha}}\frac{Z_\alpha}{u_0} & M_q + M_{\dot{\alpha}} \end{pmatrix} \tag{A7}$$

where Z_α, M_α, $M_{\dot{\alpha}}$, M_q are:

$$\begin{cases} Z_\alpha = -\frac{(C_{L\alpha}+C_{D0})\bar{q}S}{m} \\ M_\alpha = C_{m\alpha}\frac{\bar{q}S\bar{c}}{I_y} \\ M_{\dot{\alpha}} = C_{m\dot{\alpha}}\frac{\bar{c}}{2u_0}\frac{\bar{q}S\bar{c}}{I_y} \\ M_q = C_{mq}\frac{\bar{c}}{2u_0}\frac{\bar{q}S\bar{c}}{I_y} \end{cases} \tag{A8}$$

where $\bar{q}$ represents dynamic pressure, S represents wing area, $\bar{c}$ represents mean aerodynamic chord, u_0 represents cruise speed, and C_{ij} represents aerodynamic derivatives.

$$A_{RE-1} = \begin{pmatrix} {u_0}^{-1} & 0 \\ 0 & 1 \end{pmatrix} {M_R}^{-1}R_1K_{AE}x_E \tag{A9}$$

where M_R represents the mass matrix of longitudinal rigid body motion; K_{AE} represents the aerodynamic stiffness matrix of the wing and can be calculated by the vortex lattice method [42]. M_R can be expressed as

$$M_R = \begin{pmatrix} m & 0 \\ 0 & I_y \end{pmatrix} \tag{A10}$$

where m represents the total weight of the aircraft, and I_y represents the moment of inertia of the aircraft on the O_by_b axis of the body coordinate system.

Assuming that the membrane wing is defined as a three-node, two-beam element structure, as shown in Figure A1, R_1 can be expressed as

$$R_1 = \begin{pmatrix} 1 & 0 & 0 & 1 & 0 & 0 \\ -1.4c & 0 & 1 & -1.8c & 0 & 1 \end{pmatrix} \tag{A11}$$

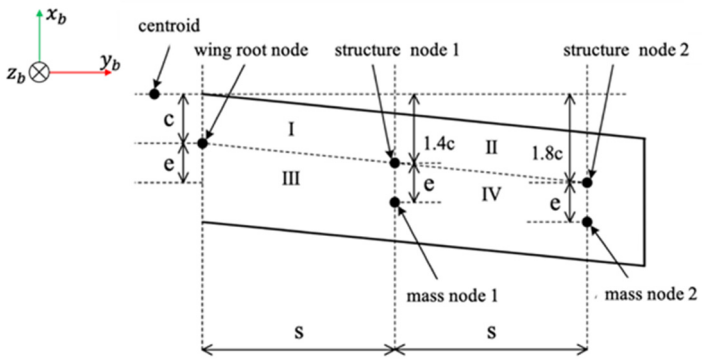


Figure A1. The finite element model of a flexible wing structure. (c, 1.4c, 1.8c represent the distance between each structure node and the centroid on the O_bx_b axis of the body coordinate system, e represents the distance between each structure node and mass node on the O_bx_b axis of the body coordinate system, s represents the distance between each structure node and wing root node on the O_by_b axis of the body coordinate system).

$$A_{EE} = \begin{pmatrix} 0 & I \\ -M^{-1}(K - K_{AE}) & -M^{-1}D_S \end{pmatrix} = \begin{pmatrix} 0 & I \\ A_{EE-21} & A_{EE-22} \end{pmatrix} \tag{A12}$$

$$A_{ER} = \begin{pmatrix} 0 \\ M^{-1}A_{RM} \end{pmatrix} = \begin{pmatrix} 0 \\ A_{ER-2} \end{pmatrix} \tag{A13}$$

where M represents the mass matrix of the wing and can be calculated by the beam model [37], K represents the stiffness matrix of the wing and can be calculated by the beam model [37], D_S represents the structural damping matrix of the wing, and A_{RM} represents the aerodynamic calculation matrix for rigid body motion and can be calculated by the vortex lattice method [42].

Appendix A.4. Parameters of the Aircraft

Table A3. Parameters of aircraft.

Category	Specific Parameter	Value
Geometry and aerodynamic parameters	Wingspan	2 (m)
	Chord length	0.2 (m)
	Wing sweep angle	5.7 (°)
	Wing dihedral angle	0 (°)
	Tail-plane area	0.0896 (m^2)
	Distance from tail pivot to CG	0.45 (m)
	Tail center of press	On the pivot axis line
	Lift coefficient slope	6.28 (rad^{-1})
	Pitching moment coefficient slope (relative to elastic axis)	0.83 (rad^{-1})
	Drag coefficient	Lift-to-drag ratio 0.2
AGAD	Pivot axis location	15% chord position
	Area	0.04 (m^2)
	Mass	0.1 (kg)
	Relative position of concentrated mass to pivot	Coincides with the end of the pivot axis
	Moment of inertia about pivot axis	$I_y = 1.921 \times 10^{-4}$ ($kg \cdot m^2$)

Table A3. *Cont.*

Category	Specific Parameter	Value
Flexible wing structure	Elastic axis location	40% chord position
	Aerodynamic center location of wing segment	30% chord position
	Wing deformation degrees of freedom	Bending deformation, torsional deformation
	Bending stiffness, EI, of wing segment	115.7 ($N \cdot m^2$)
	Torsional stiffness, GJ, of wing segment	13.83 ($N \cdot m^2$)
	Mass of wing segment	0.1 (kg)
Flight performance	Total mass	3 (kg)
	Distance from CG to wing root	0.03 m after leading edge
	Moment of inertia about $O_b y_b$ axis (body frame)	I_y = 1.04 ($kg \cdot m^2$)

Appendix A.5. Robustness Simulation

We change the amplitude of the $(1 - \cos)$ gust from 5 m/s to 10 m/s, and the shape of the gusts as shown in Figure A2.

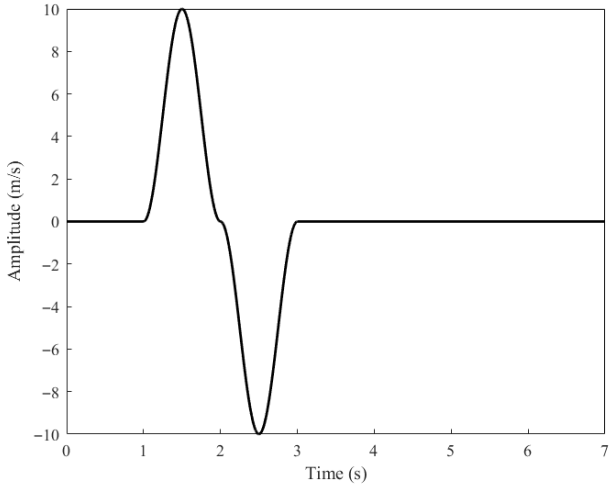


Figure A2. Gust speed during the dynamic response.

The pitch angle and wingtip twist angle of baseline control and AGAD control are shown in Figure A3.

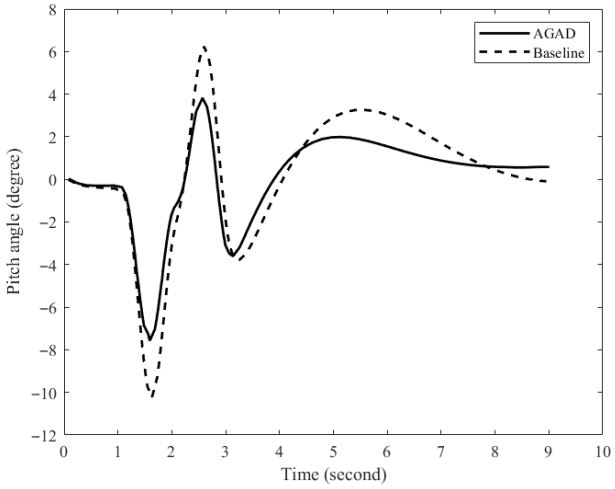


Figure A3. *Cont.*

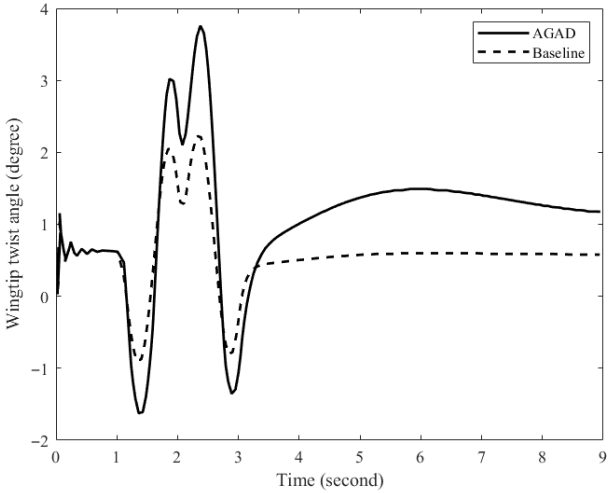


Figure A3. The pitch angle and wingtip twist angle with and without the AGAD control.

From Figure A3, we can see that the trend of variation in pitch angle and wingtip twist angle is consistent, as mentioned in the main text. Under gust disturbances, the AGAD can utilize a larger wingtip twist angle (increased by 68.6% compared to baseline control) to suppress pitch angle variation (decreased by 38.68% compared to baseline control), thereby stabilizing aircraft motion. This can help illustrate that the AGAD control proposed has robust performance.

References

1. Song, F.; Yan, Y.; Sun, J. Review of insect-inspired wing micro air vehicle. *Arthropod Struct. Dev.* **2023**, *72*, 101225. [CrossRef] [PubMed]
2. Li, F.; Bai, P.; Liu, Q. Discussion about the laminar separation theory at low Reynolds numbers. *Phys. Gases* **2017**, *2*, 1–10. [CrossRef]
3. Kay, N.J.; Richards, P.J.; Sharma, R.N. Low-Reynolds number behavior of the leading-edge suction parameter at low pitch rates. *AIAA J.* **2022**, *60*, 1721–1729. [CrossRef]
4. Guo, S.; Li, H.; Zhou, C.; Zhang, Y.; He, Y.; Wu, J. Analysis and experiment of a bio-inspired flyable micro flapping wing rotor. *Aerosp. Sci. Technol.* **2018**, *79*, 506–517. [CrossRef]
5. Lv, B.; Zha, J.; Zeng, K.; Guo, H.; Yu, L.; Zhang, P. Recent Progress on Aeroelasticity of High-Performance Morphing UAVs. *Comput. Model. Eng. Sci.* **2022**, *133*, 1–29. [CrossRef]
6. Wang, Z.; Yang, D.; Guo, S. Active control using control allocation for UAVs with seamless morphing wing. In Proceedings of the Third International Conference on Smart Materials and Nanotechnology in Engineering, Shenzhen, China, 11–13 November 2011. [CrossRef]
7. Wang, Q.; Stengel, R.F. Robust nonlinear flight control of a high-performance aircraft. *IEEE Trans. Control Syst. Technol.* **2005**, *13*, 15–26. [CrossRef]
8. Shearer, C.M.; Cesnik, C.E.S. Nonlinear flight dynamics of very flexible aircraft. *J. Aircr.* **2007**, *44*, 1528–1545. [CrossRef]
9. Ducard, G.J.J. *Fault-Tolerant Flight Control and Guidance Systems: Practical Methods for Small Unmanned Aerial Vehicles*; Springer: London, UK, 2009; pp. 229–240. [CrossRef]
10. Palacios, R.; Murua, J.; Cook, R. Structural and aerodynamic models in nonlinear flight dynamics of very flexible aircraft. *AIAA J.* **2010**, *48*, 2648–2659. [CrossRef]
11. Gamble, L.L.; Inman, D.J. Aeroelastic Design and Analysis of a Bioinspired Flexible Airfoil. In Proceedings of the AIAA Scitech 2020 Forum, Orlando, FL, USA, 6–10 January 2020. [CrossRef]
12. Waszak, M.; Davidson, J.; Ifju, P. Simulation and flight control of an aeroelastic fixed wing micro aerial vehicle. In Proceedings of the AIAA Atmospheric Flight Mechanics Conference and Exhibit, Monterey, CA, USA, 5–8 August 2002. [CrossRef]
13. Mujahid, A.; Garcia, H.; Lind, R. Flight characteristics of shaping the membrane wing of a micro air vehicle. *J. Aircr.* **2005**, *42*, 131–137. [CrossRef]
14. Bret, S.; Ijfu, P.; Albertani, R.; Shyy, W. Fixed membrane wings for micro air vehicles: Experimental characterization, numerical modeling, and tailoring. *Prog. Aerosp. Sci.* **2008**, *44*, 258–294. [CrossRef]

15. Siqueira Versiani, T.d.S.; Silvestre, F.J.; Guimaraes Neto, A.B.; Rade, D.A.; Silva, R.G.A.d.; Donadon, M.V.; Bertolin, R.M.; Silva, G.C. Gust load alleviation in a flexible smart idealized wing. *Aerosp. Sci. Technol.* **2019**, *86*, 762–774. [CrossRef]
16. Binder, S.; Wildschek, A.; De Breuker, R. The interaction between active aeroelastic control and structural tailoring in aeroservoelastic wing design. *Aerosp. Sci. Technol.* **2021**, *110*, 106516. [CrossRef]
17. Schildkamp, R.; Chang, J.; Sodja, J.; De Breuker, R.; Wang, X. Incremental Nonlinear Control for Aeroelastic Wing Load Alleviation and Flutter Suppression. *Actuators* **2023**, *12*, 280. [CrossRef]
18. Rösner, H.; Jockel-Miranda, K. Airbus Airframe—New Technologies and Management Aspects. *Mater. Und Werkst.* **2006**, *37*, 768–772. [CrossRef]
19. Guo, S.; Li, D.; Sensburg, O. Optimal design of a passive gust alleviation device for a flying wing aircraft. In Proceedings of the 12th AIAA Aviation Technology, Integration, and Operations (ATIO) Conference and 14th AIAA/ISSMO Multidisciplinary Analysis and Optimization Conference, Indianapolis, IN, USA, 17–19 September 2012. [CrossRef]
20. Zhou, Y.; Wu, Z.; Yang, C. Intelligent feedforward gust alleviation based on neural network. *Chin. J. Aeronaut.* **2024**, *37*, 116–132. [CrossRef]
21. Nguyen, N.T.; Urnes, J. Aeroelastic Modeling of Elastically Shaped Aircraft Concept via Wing Shaping Control for Drag Reduction. In Proceedings of the AIAA Atmospheric Flight Mechanics Conference, Minneapolis, MN, USA, 13–16 August 2012. [CrossRef]
22. Nguyen, N.T.; Trinh, K.; Reynolds, K.; Kless, J.; Aftosmis, M.; Urnes, J. Elastically Shaped Wing Optimization and Aircraft Concept for Improved Cruise Efficiency. In Proceedings of the 51st AIAA Aerospace Sciences Meeting including the New Horizons Forum and Aerospace Exposition, Grapevine, TX, USA, 7–10 January 2013. [CrossRef]
23. Ippolito, C.; Nguyen, N.T.; Totah, J.; Trinh, K.; Ting, E.B. Initial Assessment of a Variable-Camber Continuous Trailing-Edge Flap System for Drag-Reduction of Non-Flexible Aircraft in Steady-State Cruise Condition. In Proceedings of the AIAA Infotech@Aerospace (I@A) Conference, Boston, MA, USA, 19–22 August 2013. [CrossRef]
24. Nguyen, N.T.; Livne, E.; Precup, N.; Urnes, J.M.; Nelson, C.; Ting, E.; Lebofsky, S. Experimental Investigation of a Flexible Wing with a Variable Camber Continuous Trailing Edge Flap Design. In Proceedings of the 32nd AIAA Applied Aerodynamics Conference, Atlanta, GA, USA, 16–20 June 2014. [CrossRef]
25. Lebofsky, S.; Ting, E.; Nguyen, N.T.; Trinh, K.V. Aeroelastic Modeling and Drag Optimization of Flexible Wing Aircraft with Variable Camber Continuous Trailing Edge Flap. In Proceedings of the 32nd AIAA Applied Aerodynamics Conference, Atlanta, GA, USA, 16–20 June 2014. [CrossRef]
26. Nguyen, N.T.; Cramer, N.B.; Hashemi, K.E.; Drew, M.C.; Xiong, J.; Mundt, T.; Mor, M.; Livne, E.; Ting, E.; Dao, T.; et al. Progress on Gust Load Alleviation Wind Tunnel Experiment and Aeroservoelastic Model Validation for a Flexible Wing with Variable Camber Continuous Trailing Edge Flap System. In Proceedings of the AIAA Scitech 2020 Forum, Orlando, FL, USA, 6–10 January 2020. [CrossRef]
27. Berg, J.; Ting, K.-Y.; Mundt, T.J.; Mor, M.; Livne, E.; Morgansen, K.A. Exploratory Wind Tunnel Gust Alleviation Tests of a Multiple-Flap Flexible Wing. In Proceedings of the AIAA Scitech 2022 Forum, San Diego, CA, USA; Virtual, 3–7 January 2022. [CrossRef]
28. Healy, F.; Cheung, R.; Rezgui, D.; Cooper, J.; Wilson, T.; Castrichini, A. Experimental and Numerical Nonlinear Stability Analysis of Wings Incorporating Flared Folding Wingtips. *J. Aircr.* **2024**, *61*, 140–154. [CrossRef]
29. Ahmadi Tehrani, M.; Ellis, J.; Farsadi, T.; Jiffri, S.; Khodaparast, H.H.; Friswell, M. Experimental Active Gust Load Alleviation via an Actuated Wingtip. In Proceedings of the AIAA SCITECH 2025 Forum, Orlando, FL, USA, 6–10 January 2025.
30. Han, J.; Wu, Z.; Yang, C. Nonlinear Aeroelastic Response Analysis of Wing with Flared Folding Wingtip. *J. Aerosp. Eng.* **2024**, *37*, 04024013. [CrossRef]
31. Balatti, D.; Ellis, J.; JiffrI, S.; Khodaparast, H.H.; Friswell, M.I. Active hinged wingtip for gust load alleviation and manoeuvres. In Proceedings of the AIAA SCITECH 2023 Forum, National Harbor, MD, USA, 23–27 January 2023. [CrossRef]
32. Narimani, M.; Haddadpour, H.; Pourtakdoust, S.H. Model predictive control of a flared folding wingtip for gust load alleviation. *Aerosp. Sci. Technol.* **2025**, *159*, 109992. [CrossRef]
33. Gao, W.; Liu, Y.; Li, Q.; Lu, B. Gust load alleviation of a flexible flying wing with linear parameter-varying modeling and model predictive control. *Aerosp. Sci. Technol.* **2024**, *155*, 109671. [CrossRef]
34. Silvestre, F.J.; Guimarães Neto, A.B.; Bertolin, R.M.; Silva, R.G.A.d.; Paglione, P. Aircraft control based on flexible aircraft dynamics. *J. Aircr.* **2017**, *54*, 262–271. [CrossRef]
35. Mohamed, M.; Madhavan, G. Reduced order model based flight control system for a flexible aircraft. *IFAC-PapersOnLine* **2020**, *53*, 75–80. [CrossRef]
36. Sy, P.H.; Ahn, K.K. Disturbance Attenuation-Based Global Integral Sliding mode Control of an Electro-Hydraulic system With Precribed Performance. *IEEE Access* **2024**, *12*, 105108–105118. [CrossRef]
37. Wright, J.; Cooper, J. *Introduction to Aircraft Aeroelasticity and Loads*; AIAA Education Series; American Institute of Aeronautics and Astronautics: Reston, VA, USA, 2007; pp. 395–413.
38. Waszak, M.R.; Schmidt, D.K. Flight dynamics of aeroelastic vehicles. *J. Aircr.* **1988**, *25*, 563–571. [CrossRef]

39. Majeed, M.; Jatinder, S. Frequency and time domain recursive parameter estimation for a flexible aircraft. *IFAC Proc. Vol.* **2013**, *46*, 453–458. [CrossRef]
40. Mohamed, M.; Swaroop, S. Model simplification methods for a reduced order system of flexible aircraft. In Proceedings of the 2015 International Conference on Control, Instrumentation, Communication and Computational Technologies, Kumaracoil, India, 18–19 December 2015. [CrossRef]
41. Looye, G.H.N. An Integrated Approach to Aircraft Modelling and Flight Control Law Design. Ph.D. Thesis, Delft University of Technology, Delft, The Netherlands, 2008.
42. McBain, G.D. *Theory of Lift*; John Wiley & Sons: Chichester, UK, 2012; pp. 209–222. [CrossRef]
43. Wu, Y.; Fu, Y.; Wang, Z.; Yu, Y.; Li, H. Scheduling Control Considering Model Inconsistency of Membrane-Wing Aircraft. *Processes* **2025**, *13*, 2367. [CrossRef]
44. Han, J.Q. From PID to active disturbance rejection control. *IEEE Trans. Ind. Electron.* **2009**, *56*, 900–906. [CrossRef]
45. Li, L.; Wang, H.; Cui, L. Attitude Control of Flapping Wing Aircraft Based on Energy Optimization and ESO. *Biomim. Intell. Robot.* **2021**, *1*, 100005. [CrossRef]
46. Cheng, H.; Zhang, S.; Feng, Y.; Fu, W.; Ni, M. Observer-Based Optimized Backstepping Control Using Critic-Actor Reinforcement Learning for Morphing Aircraft. *Aerosp. Sci. Technol.* **2025**, *164*, 110388. [CrossRef]

Disclaimer/Publisher's Note: The statements, opinions and data contained in all publications are solely those of the individual author(s) and contributor(s) and not of MDPI and/or the editor(s). MDPI and/or the editor(s) disclaim responsibility for any injury to people or property resulting from any ideas, methods, instructions or products referred to in the content.